A Solar Absorber Based on
Metal Nanoparticles

Håkon Eidsvåg

Master's Thesis in Energy

Supervisor: Professor Dr. Bodil Holst
Co-supervisor: Dr. Martin Møller Greve
Co-supervisor: Ranveig Flatabø

Department of Physics and Technology
University of Bergen

June, 2016

Abstract

Metal nanoparticles (MNPs) exhibits unique optical properties often found in the visible spectrum of light. The key point of interest is the so-called Localized Surface Plasmon Resonance (LSPR) effect, that arises within particles exposed to electromagnetic radiation. An increase in scattering and absorption of light can be seen for specific wavelengths of incident electromagnetic radiation due to the LSPR effect. Through tuning of the nanoparticle size, shape, interparticle distance and metal, the LSPR wavelength and absorption spectra for the MNPs can be manipulated. However, a solar absorber purely based on MNPs and their LSPR has not been designed yet. In this work a suitable basis is shown for making solar absorbers solely based on individual MNPs and a design for the solar absorber is presented. The LSPR wavelengths dependency on particle size, shape and metal were confirmed through a series of experiments. Gold and aluminium MNP arrays consisting of decoupled particles with diameters in the range of 40 nm - 200 nm were fabricated by the means of electron beam lithography. In addition mixed arrays consisting of particles with varying sizes and metals were fabricated. The extinction and absorption spectra measured from the MNP arrays were found to match published literature. The optical analyses of the arrays revealed that the maximum extinction is highly dependent on surface coverage. In addition to the fact that the peak position can be fine-tuned by changing the particle diameter. It was also found that aluminium has a broader extinction peak than gold, making it an ideal candidate for broad band light absorption. Our results demonstrate how MNPs can be used to design a solar absorber, which could absorb over a larger spectrum than conventional solar energy converters. The work done in this thesis provides a foundation for further research and optimization of MNPs in solar absorbers.

Acknowledgements

Contents

List of Figures

List of Tables

Chapter 1

Introduction

1.1 Background

In 2009 at the Conference of the Parties (COP) in Copenhagen the United Nations recognised climate change and global warming as one of the greatest challenges of our time [1]. This was backed up in September 2013 by the Intergovernmental Panel on Climate Change stating that the level of greenhouse gases in the atmosphere has not been higher in the last 800 000 years [2]. The primary greenhouse gases are water vapour (H_2O), carbon dioxide (CO_2), methane (CH_4), nitrous oxide (N_2O) and ozone (O_3) [2], which also makes these gasses the leading contributors to the greenhouse effect.
Although the greenhouse effect is critical for life on earth, a considerable increase can lead to irreversible climate changes. Essentially the greenhouse gasses absorbs thermal radiation from earth. This is then radiated out in all directions as infrared (IR)-radiation, and an increase of greenhouse gases will lead to more radiation being trapped and emitted down to earth again [2]. A build up of greenhouse gases will enhance the natural greenhouse effect and as a consequence temperature will rise. Too avoid irreversible climate change the COP agreed on a 2°C limit as the maximum temperature increase [1]. In 2015 the COP21 was arranged in Paris and during this conference they lowered the maximum temperature rise to 1.5°C [3]. This change emphasises the severity of global warming, and the importance of reaching the goal. Achieving this goal will require a change in energy consumption, politics and resources.
In 2013 more than 80% of the used fuel in the world was fossil fuels, while renewable accounted for 8.9% [4]. In Figure 1.1 we see that the current contribution from renewable energy is almost negligible, except for hydroelectricity. The potential from other renewable are great, especially from solar based energy. A recent study at MIT shows that the entire worlds energy consumption in 2050 can be covered by solar-based energy [5]. Solar-based energy can be divided into two main categories: solar cells and solar absorbers. In a solar cell the incoming radiation is converted into electricity through the photovoltaic effect, which is explained in Section 1.2. Solar absorbers on the other hand generate heat through absorption of the incoming solar radiation. At the moment solar-based energy is experiencing a major growth due to a heavy subsidised market [6]. This subsidising will eventually stop, and as long as solar-based energy relies on subsidies for being competitive with fossil fuel, it can not be viewed as sustainable. To overcome this barrier further research in conversion efficiency, material and production cost is essential. The aim of this thesis is to create a solar absorber based on metal nanoparticles (MNPs). The advantage of the proposed technology is the potential high efficiency, potentially low production costs and the fact that solar absorbers are simple to apply. The high efficiency comes from utilising MNPs and their solar absorption capabilities. The full scale arrays are planned to be produced by sputter coating, which is a cost-effective technique. Because the absorption layer itself will be very thin (less than

1 micron), it will in theory be simple to apply this type of solar absorber to buildings and other constructions. The general principle behind solar cells and solar absorbers will now be discussed to get an overview of the general solar-based energy field.
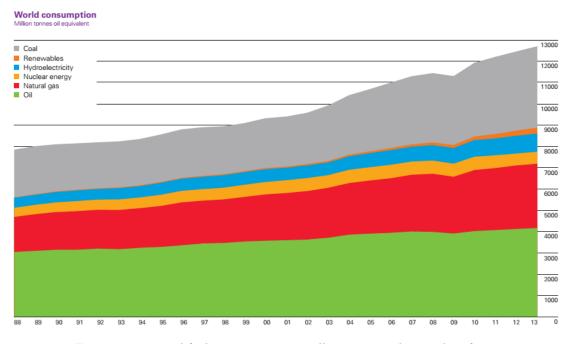
FIGURE 1.1: Total fuel consumption in million tonnes oil equivalent from 1988 to 2013. The figure is taken from [4].

1.2   Solar Cells

The first observations of electrical currents being induced by light were by Alexandre Edmund Becquerel in 1839 [7]. Becquerel illuminated platinum electrodes coated with AgCl or AgBr submerged in an acidic solution. In the following years scientists discovered similar effects from other materials, among them solids like selenium. This phenomenon is called the photovoltaic effect, and is the fundamental process for all modern solar cells. The vast majority of today's solar cells integrate a semiconductor in their design [8]. The semiconductors can be doped to change their electrical properties and be tuned for the photovoltaic effect. Doping is achieved by adding another material to the silicon which changes the carrier concentration and increases the conductivity. The dopant atoms can either increase the amount of free electrons in the conduction band (negative doping, donor) or add free holes in the valence band (positive doping, acceptor) [9]. When these two layers are combined (Figure 1.2) electrons in the donor will travel to the acceptor and recombine with the holes there, and vice versa. This charge transfer leaves behind an excess of negatively charged ions in the acceptor and an excess of positively charged ions in the donor. These charged ions will set up an electric field which maintains the separation of the two carriers. The electric field creates a zone effectively free of charge, named the depletion layer [10]. This is called a p-n junction semiconductor and is depicted in Figure 1.2.
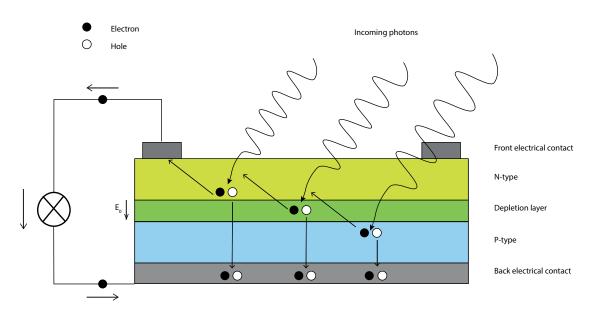
FIGURE 1.2: A semiconductor with a p-n junction, where the p-n juction consists of one p- and one n-doped layer. A positive doped layer (P-type) is termed an acceptor, while a negative doped layer (N-type) is termed the donor. Incoming photons will be absorbed in the various layers depending on their energy, creating an electron-hole pair. The electron will be attracted to the positive charge in the donor, while the holes will be attracted to the negative charge in the acceptor. In the donor the electrons will repel each other as they have equal charge. Therefore, by connecting the N-type to the P-type the electrons are provided a way to move away from each other. Hence, an electrical current is created.

For a photovoltaic cell to generate energy via electron-hole pairs the incoming electromagnetic radiation must coincide with the band gap of the semiconductor. The band gap is defined as the energy needed to excite an electron from the valence band to the conduction band. In other words, it is the minimum energy required to remove an electron from a covalent bond so that it may roam the semiconductor freely and contribute to the electrical current. Therefore, the incoming photon must have energy equal to that of the band gap

$$h\nu = E_{bg}.$$

Where h is Planck's constant, ν is the frequency of the photon and E_{bg} the band gap energy. Accordingly, when a photons energy is less than the band gap the excited electrons will not have enough energy to reach the conduction band. Therefore, they can not contribute to the electrical current. On the other hand if the photon energy is greater than that of the band gap an electron could be excited and move freely in the semiconductor, but the excess energy will be lost as heat. The detailed balance limit calculated by Shockley and Queisser in 1961 [11] states that the maximum theoretical limit for a silicon p-n junction solar cell is 33.7 %. There are three major contributors to this limit. As mentioned earlier, when an incoming photon has a higher energy than needed to excite the electron, the excess energy is lost as heat radiation in the cell. In an ideal cell every photon with the correct energy would generate an electron-hole pair, but according to the detailed balance limit the reverse might occur as well. That is an electron and a hole recombining and emitting a photon, thus reducing the efficiency. However, the largest contributor to the detailed balance limit is due to spectrum losses. As only a certain amount of the incoming photons will have the appropriate energy

levels to excite an electron high enough, about 53 % of the energy that enters the cell will be lost [12]. It should be noted that the limit is calculated for the solar spectrum.

1.3   Nanoparticle Solar Cells Technologies

Although the discovery of the photovoltaic effect was done decades earlier, it was not until 1954 that the first silicon solar cell was built by Chapin [13]. The majority of today's solar cells are first generation silicon cells, ranging from single layer monocrystalline to multi-junction polycrystalline [14]. Material cost and efficiency limits have forced forward new generations, which to a large extent are based on different working principles and materials rather than semiconductors. Especially the third generation of solar cells are looking at new possibilities of utilizing the photovoltaic effect, many of which are based on nano -particles and -structures.

1.3.1   Nanoparticles in Si solar cells

The current major use of nanoparticles in standard Si solar cells is as efficiency enhancements. By utilizing nanoparticles the goal is to overcome the detailed balance limit. There are several ways to achieve this, and two promising methods are by improving light trapping in the cell or by implementations of quantum wells.

Light Trapping

In the pursuit of reduced material cost for solar cells the thickness of the silicon wafer is reduced. Unfortunately reducing the thickness also lowers the solar absorption efficiency of the solar cell. This setback can be avoided by the technique called light trapping. The basic idea of this approach is to make the optical path length through the cell much longer than the cell thickness [15]. Where the optical path length is the product of the geometric length the light travels through the system and the index of refraction of the medium in which the light propagates. A p-i-n junction, which is a p-n junction with an undoped intrinsic region between the doped layers, is placed on a back reflector(BR). Light passing through the p-i-n junction, without being absorbed, is then scattered by the BR and thus increasing the amount of light in the cell.

Quantum Wells

Another technique to increase the efficiency of first generation solar cells is to utilize quantum wells. The quantum wells are made out of lower bandgap materials, and are placed in between the p-n layers, making it a p-i-n structure. The reasoning behind the idea is to move the absorption edge of the solar cell closer to the optimal value, without any buffer layer between the absorbing layer and the substrate [16]. A quantum well cell is a multiple band-gap device with properties between heterojunction cells and tandem cells [16]. It has been shown that quantum well solar cells can enhance the efficiency of cells of the same material [16].

1.3.2   Carbon Nanotubes

Carbon nanotubes can be put into two categories, single-walled or multi-walled. The single-walled nanotube consists of a single layer of graphene, while the multi-walled nanotubes consists of multiple layers of graphene.

Carbon nanotubes can either be metallic or semiconducting with first-class mechanical and electronic properties. The electronic properties is utilised in the creation of solar cells. A p-n junction semiconductor is created by coating nanotubes with special p and n type materials, before joining them together [17]. With this method an increase in surface area is experienced, leading to an enhanced electricity production. In a regular solar cell the detailed balance limit is calculated by Shockley and Queisser, due to the conversion of a single photon into a single electron-hole pair. For a single-walled nanotube on the other hand, a single photon is converted into multiple electron-hole pairs, leading to increased efficiency and the possibility of surpassing the limit established by Shockley and Queisser, this does however require a lot of research before it can be utilised [18]. Today carbon nanotubes are used as the transparent electrode for efficient, flexible polymer solar cells [17].

1.3.3 Quantum Dots

Quantum dots (QD) are nano sized particles made from semiconducting materials. By adjusting the diameters of the QDs it is possible to tune the absorption band-gap of the particles. A larger and wider band-gap will lead to absorption of high energetic photons, which means a low current but a hight output voltage. On the other hand, a small band-gap would absorb low energetic photons and therefore produce a larger current but smaller output voltage [19]. It was shown by Luque and Martí that the efficiency for quantum dot solar cells with an intermediate band of states are as high as 63.1% [20]. These solar cells are made by introducing single-sized dots into an ordered array within the intrinsic region of a p-i-n solar cell [8].

1.3.4 Hot Carrier Cells

One of the greatest energy losses in a solar cell is attributed to radiation of heat in the solar cell. Hot carrier solar cells tries to exploit this heat before it dissipates, making it the most intricate technology of the third and fourth generation solar cells [19]. The reason why this is so hard is because the carriers (electrons and holes) now have to be captured before the carrier cooling stage. This can either be achieved by reducing the cooling rates or force the carriers to travel through the cell very quickly. The theoretical efficiency for hot carrier cells is 86.8% [14].

1.4 Solar Absorbers

Solar absorbers are also often known as solar thermal collectors or solar collectors, although in this work the term solar absorber will be used. The goal of a solar absorber is to absorb all visible light radiated from the sun which reaches earth's surface.

1.4.1 Flat Plate Collectors

Flat plate collectors are the elementary form of solar absorbers. They consist of an absorber plate, an insulated underside, flow tubes and a sheet of glass. The plate absorber absorbs incoming light and converts it into heat. This heat is then transferred to the transport liquid that is located in the flow tubes. Often water is used as a transport liquid, but regions where the temperature can drop below zero degrees has to utilise an antifreeze solution. Otherwise major structural damage could occur due to freezing of the fluid. The sheet of glass covering the absorber allows short wave

solar radiation to easily enter, but it also traps long wave radiation radiated from the absorber. A well insulated underside is of high importance to prevent substantial heat losses through the underside [21]. The heated fluid is pumped through a boiler, in which a heat exchange will occur. The transported heat will be transferred over to the water in the boiler. Therefore, warm water can be stored for longer periods of time and always utilised when needed. To prevent lose of heat to the surroundings at night or when the sun is gone, the system is equipped with a pump that controls the water flow through the system.

1.4.2   Evacuated Tube Collectors

Increased efficiency and reduced thermal losses can be achieved by employing a vacuum between the plate and cover. The vacuum gets rid off the convective and conductive heat losses. Flat plate collectors are not suited as evacuated collectors as their structure does not withstand the vacuum properly. Therefore, a cylindrical geometry is used to obtain a greater structural strength [21]. The collector consists of several heat pipes in which heat is transported rapidly up the tube by the means of a phase change. Inside every vacuum sealed pipe a volatile liquid is heated by the incident solar radiation and vaporized. The hot vapour travels up the length of the tube and into the canula, a bulb at its end. A pipe circumferences the canula, where water flows through this pipe and gets heated by the hot vapour in the canula [21]. The vapour is then condensed back to its liquid state and due to gravity finds it way back down in the tube, where the process can start anew.

1.4.3   Solar Power Tower

The solar tower design utilises an high amount of mirrors on the ground which tracks the sun and concentrates the sunlight onto the top of the tower. Inside that top region a fluid is placed, which is heated by the concentrated sun light. Usually liquid fluoride molten salts are used instead of water, making it possible to achieve temperatures up to 800 $^\circ C$ [21]. The molten salts is stored in large underground tanks, where the heat is used to drive steam-driven generators. Storing the energy like this makes it possible to utilise it during night as well, reducing the intermittency problem solar energy experience. Instead of using the energy to power steam turbine it can be directed through optical fibres and used as illumination in domestic homes.

1.4.4   Parabolic Dish/Trough

Rather than focusing the solar energy with numerous mirrors to one single point, a parabolic trough/dish can focus the energy at their focal point. Achieving maximum efficiency requires solar tracking to make sure the greatest amount of radiation is at all time focused at the focal point. The parabolic troughs can only focus the radiation in one dimension. Hence, the single tracking requirement is to match the troughs angle to the sun's elevation angle. On the other hand, parabolic dishes can focus the incoming radiation in two dimensions [21]. Therefore, one also has to track the hour angle of the sun as well as the elevation angle. Two dimensional systems can achieve a higher temperature, but the tracking is more difficult to implement correctly. A small pipe/container is placed near the focal point where a fluid is heated. The fluid is then guided through a pipe system until it reaches the central storage where it can power steam turbines.

1.4.5 Metallic Dielectric Photonic Crystals

Moving away from the classical approach of heating a fluid with the incoming radiation, research has been focused on using advanced material science to absorb the solar spectrum. At MIT such a device has recently been constructed (in 2014) and named a "perfect" solar absorber [22]. Chou et al developed a 2D metallic dielectric photonic crystal with solar broadband, omni-directional and tunable selective absorption with high temperature stable properties on a silicon wafer [22]. The basic idea is to create nanocavities on a silicon wafer, these are then filled with HfO_2, a dielectric material. When sun light strikes the absorber, the radiated light will be absorbed and the material will start to glow. This will then emit light which can be converted into an electric current. Hence the crystal works as a solar thermophotovoltaic, a hybrid consisting of a solar absorber and a solar cell. In other words, the light emitted from the crystal is emitted at tailored wavelength which is just above the band gap for the connected solar cell [23][24]. The advantage of this technology is that absorption spectra can be tuned by changing the size or material of the nanocavities [22]. The crystal can be fabricated on a large scale with the current technology, it also utilises non expensive materials making it a low cost alternative. Mirrors would still be used to focus the incoming radiation, this is to enhance the efficiency. Therefore, the absorber was built to have a high temperature durability. As the materials in the absorber is interchangeable, metals with high heat endurance can be implemented. Lastly the device was shown to absorb sunlight efficiently from a wide range of incident angles, making solar tracking unnecessary.

1.4.6 Light Absorption with Metal Nanoparticles (MNPs)

Light absorption with metal nanoparticles are done through the phenomenon termed localized surface plasmon resonance (LSPR), which will be discussed in more details in Chapter 2. However, a general definition will be provided for the following sections. Metal nanoparticles placed in a electromagnetic field will experience an oscillation of their conduction electrons. Given that the diameter of the MNPs is smaller than the wavelength of the field, the surface of the particles will exert a restoring force on the electrons. This restoring force gives rise to a resonance and the simplest way to look at LSPR is as an oscillator. LSPR is one of two main ingredients in the field termed plasmonics, which covers processes between electromagnetic radiation and conduction electrons at metallic interfaces or in small metallic nanostructures, leading to an enhancement in optical properties [25]. The use of LSPR in solar absorbers has increased in the past years, although mainly implemented as efficiency enhancing parts in state of the art photovoltaic technology [26]. Progress has been made in creating solar absorbers utilising LSPR independently, where the major contributions have come from the developing of LSPR sensors or antennas. This is discussed below.

Localized Surface Plasmon Sensors

In the field of bio/chemosensors LSPR sensors have been under development for a while, resulting in nearly perfect absorbers at given wavelengths. One such sensor was developed by Liu et al. [27]. Liu et al. developed a perfect LSPR absorber (99% absorbency at normal incidence) at $\lambda = 1.6$ μm which was polarization independent [27]. The sensor structure is placed on top of a glass wafer and consists of a gold mirror, a spacer layer and nano gold disks. It is within these disks the absorption occurs and this gives rise to localized surface plasmon resonance which can be utilised to extract a electrical current.

Although LSPR are used only for their absorption capabilities in sensors it showcases the potential of LSPR solar absorbers and the importance of future research in this field.

Localized Surface Plasmon Resonance Super Absorber

In the recent years interest in nanostructured solar absorbers have increased, leading to the development of an ultra thin LSPR super absorbers [28]. Crossed silver trapezoid arrays were placed on a silicon oxide layer which rested on a silver layer. Both silver layers were 100 nm thick, while the SiO_2 layer was 60 nm thick. Trapezoid arrays was chosen as a symmetric arrangement due to the fact that their geometry would exclude the independence of polarisation for the incoming light. Thus, the averaged absorption of 71% is independent of the incident polarisation [28] and valid within the experimental tested spectral range of 400 nm - 700 nm. The absorber is designed to absorb light in the metallic sections, therefore the energy is converted to heat. In other words, it works as a thermophotovoltaic cell where the heat must be utilised to get electricity as the output. The authors claims that by replacing the dielectric spacer (SiO_2) with an active semiconductor this could result in broadband absorption and photocarrier generation [28].

1.5   Thesis Objective

- The overall aim of this thesis is to contribute towards the design of an effective broad band solar absorber based on metal nanoparticles. This will be done in the following way:

- By using an already established electron lithography method [29][30] to produce a range of nanoparticle arrays of gold and aluminium with well defined size and distance and investigate their absorption properties using integrating sphere spectroscopy.

- Establish a new fabrication method for making samples with nanoparticles of various sizes predetermined and in a predetermined array using electron beam lithography and test these new mixed arrays using integrated sphere techniques. Proximity corrections and over-lay techniques are expected to be used in the fabrication process.

- On the basis of the experimental results, suggest an arrangement of metal nanoparticles on a glass substrate for absorbing the largest part of the visible spectrum. The geometry, choice of metal and particle distribution will be of importance.

1.6   Thesis Outline

Chapter 2 presents the theoretical background for localized surface plasmon resonance, spectroscopy and underlying principles for array composition. Chapter 3 gives an overview of the equipment used in sample preparation and characterisation. Chapter 4 goes through the experimental procedure of producing the nanoparticles, with particular focus on the electron beam lithography and new procedures developed during the thesis. In Chapter 5 the results from the SEM characterisation and optical measurements will be presented and discussed. The thesis will finish with a conclusion and discussion of future work in Chapter 6.

Chapter 2

Theoretical Background

This chapter presents the fundamental theory for localized surface plasmon resonance (LSPR) for metal nanoparticles (MNPs). It goes through the history of LSPR before it starts on the underlying principles for electromagnetic interactions with metals. This theory is then built on to create a foundation on which LSPR can be explained. At the end of the chapter numerical solutions to Maxwell's equations and theory behind an absorbing sample is discussed.

2.1 History of Localized Surface Plasmon Resonance

Optical properties of metals have fascinated mankind for centuries, one of the earliest examples of this is the Lycurgus cup dated to the fourth century A.D [31]. The Romans learned that by adding plant ash or mineral salts to melted glass the finished product would showcase different colours depending on the salts added. Another remarkable attribute was that the colour would change depending on the light conditions, this is called the dichroic effect. The Lycurgus cup (shown in Figure 2.1) is an prime example of this, as it is green when light is reflected off the surface and red when light is transmitted through it. To explain the phenomena one has to look at the interaction between the gold and silver nanoparticles inherent in the glass and the incoming light. This interaction is a demonstration of the localized surface plasmon resonance (LSPR) effect [25]. The theory of light as a wave was first discussed by Maxwell in 1904 [32]. Then in 1908 Mie developed an exact solution to Maxwell's equations for electromagnetic radiation by a sphere [33], providing the mathematical foundation for LSPR. This was followed by Pines in 1956 who claimed that the energy loss by electrons travelling through metals were due to plasmon excitations [34]. Ritchie proved in 1957 that plasmons can be excited near the surface of metals [35], while in 1970 Kreibig and Zacharias used plasmons to describe the optical properties of metal nanostructures [36]. Current research on localized surface plasmon resonance are spread between a wide variety of disciplines, varying from biosensing to photvoltaics [37].

9

(A) Light reflected by the Lycurgus cup   (B) Light transmitted through the Lycurgus cup

FIGURE 2.1: A) and B) shows the Lycurgus cup with two different placements of the light source, respectively in front of it (A) and behind it (B). The different colours are due to the gold and silver nanoparticles integrated in the glass. The images are taken from Håvardstun [38].

2.2 Electromagnetic Interactions with Metals

The interactions between electromagnetic fields and metals, including classical MNPs, can be fully described by Maxwell's equations. On standard form and within the classical part of physics Maxwell's equations are [25]

$$\nabla \cdot \boldsymbol{D} = \rho_{ext} \,, \tag{2.1}$$

$$\nabla \cdot \boldsymbol{B} = 0 \,, \tag{2.2}$$

$$\nabla \times \boldsymbol{E} = -\frac{\partial \boldsymbol{B}}{\partial t} \,, \tag{2.3}$$

$$\nabla \times \boldsymbol{H} = \boldsymbol{J_{ext}} + \frac{\partial \boldsymbol{D}}{\partial t} \,. \tag{2.4}$$

Where $\boldsymbol{D}$ is the dielectric displacement, $\boldsymbol{E}$ the electric field, $\boldsymbol{H}$ the magnetic field and $\boldsymbol{B}$ the magnetic induction with ρ_{ext} and $\boldsymbol{J_{ext}}$ as the external charge and current density respectively. The electromagnetic fields are related to each other through constitutive relations which are material specific. The constitutive relations can be defined as [25]

$$\boldsymbol{D} = \epsilon_0 \epsilon \boldsymbol{E} \,, \tag{2.5}$$

$$\boldsymbol{B} = \mu_0 \mu \boldsymbol{H} \,, \tag{2.6}$$

$$\boldsymbol{J} = \sigma \boldsymbol{E} \,. \tag{2.7}$$

ϵ_0 is called the permittivity of free space, ϵ is the dielectric constant or relative permittivity, μ_0 is the permeability of free space, μ is the relative permeability of the non-magnetic medium and σ is the conductivity [25]. The linear relationship in equation (2.5) indicates that $\boldsymbol{D}$ would react instantaneously to a change in $\boldsymbol{E}$ which would only be valid for a linear media that do not exhibit temporal or spatial dispersion [25]. As this does

not hold for real materials and metals, we need to take into account the non-locality of time and space. This leads us to the dielectric function

$$\epsilon(\omega) = 1 + \frac{i\sigma(\omega)}{\epsilon_0(\omega)} \ , \tag{2.8}$$

where i is the imaginary unit and ω is the angular frequency of the electric field. ϵ and σ can be divided into a real part and an imaginary part:

$$\epsilon(\omega) = \epsilon_1(\omega) + i\epsilon_2(\omega) \ , \tag{2.9}$$
$$\sigma(\omega) = \sigma_1(\omega) + i\sigma_2(\omega) \ . \tag{2.10}$$

Here subscript 1 denotes the real parts and subscript 2 denotes the imaginary parts of ϵ and σ. ϵ_1 and σ_2 are attributed to the polarisation of the medium, while ϵ_2 and σ_1 determines the absorption inside the material. The dielectric function can be experimentally determined through reflective studies and the complex refraction index

$$\tilde{n} = \sqrt{\epsilon} \ . \tag{2.11}$$

With the complex refraction index given as

$$\tilde{n} = n(\omega) + i\kappa(\omega) \ . \tag{2.12}$$

Where n is the refractive index of the medium, κ is the extinction coefficient

$$\kappa = \frac{\epsilon_2}{2n} \tag{2.13}$$

and determines the optical absorption of electromagnetic waves propagating through the medium.

2.2.1 The Drude Model

In 1900 P. Drude proposed a model to explain the observed optical properties of metals. Although a simplistic model it still plays a major role in the understanding of electrical conductivity. The model is based on the following assumptions [9]:

- The electrons in a solid are free to move around with no interactions between each other, hence there is no Coulomb interactions and the electrons do not collide with each other.

- The positive charges are fixed as stationary ion cores, with which the electrons can collide.

- It is assumed that such a scattering event would occur with the probability $\gamma = 1/\tau$, where τ is the relaxation time.

- The electrons reach thermal equilibrium with the lattice through the collisions.

This way of studying electrons is commonly known as a plasma model (i.e. a sea of free charges).

If such a plasma sea is subjected to an external electric field $\boldsymbol{E}$, with an harmonic time dependence $\boldsymbol{E}(t) = \boldsymbol{E}_0 e^{(-i\omega t)}$, the dielectric function can be derived from the

equation of motion of a single electron. From this the following can be derived

$$\epsilon(\omega) = \epsilon_1(\omega) + i\epsilon_2(\omega) = 1 - \frac{\omega_p^2}{\omega + i\gamma\omega} \ , \tag{2.14}$$

where ω_p is the so called plasma frequency of the free electron gas. ω_p is given as

$$\omega_p^2 = \frac{ne^2}{m_e\epsilon_0} \ , \tag{2.15}$$

m_e is the electron mass, e is the charge of the electron and n is the reflective index of the material. For frequencies close to ω_p damping is negligible, leading to a mainly real $\epsilon(\omega)$ and

$$\epsilon(\omega) = 1 - \frac{\omega_p^2}{\omega^2} \ . \tag{2.16}$$

This is the dielectric function of the undamped free electron plasma. From this we can see that we have two cases for ϵ, it can either be real and negative or real and positive. For $\omega < \omega_p$, ϵ is real and negative. This means that $\sqrt{\epsilon}$ is imaginary and the complex refraction index in equation (2.12) contains only the imaginary part $i\kappa$. A material with a complex valued refractive index can not support propagating waves inside itself, therefore electromagnetic waves must be reflected in this scenario. For $\omega > \omega_p$, ϵ is real and positive. Here the reflective index is real and allows propagating waves inside the medium, in other words electromagnetic waves can propagate through the metal. This is why metals are reflective for low-frequency light and turn transparent for high-frequency light. This transition occurs at the plasma frequency [9]. Aluminium, which is one the metals used in this thesis, is well described by the model. Unfortunately the Drude model fails to predict the behaviour of noble metals as their interband transitions are not accounted for. These interband transitions will occur in the range where equation (2.16) is valid [9]. As gold is of a major importance in this thesis more sophisticated models are needed, but the Drude model gives a good fundation for the following theory about localized surface plasmons.

2.3 Localized Surface Plasmon Resonance

Localized surface plasmon are non propagating oscillations of the conduction electrons in a metal nanostructure coupled to a electromagnetic field [25]. The curved surface of the particles exerts a restoring force on the electrons, giving rise to a resonance. This is what is called localized surface plasmon resonance (LSPR), and can in the simplest way be looked at as an oscillator, which is illustrated in Figure 2.2.
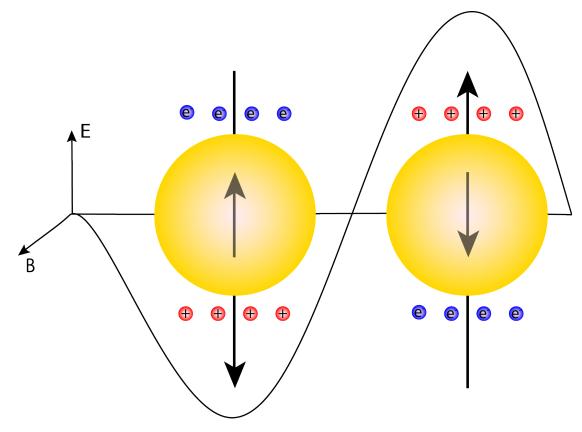
FIGURE 2.2: An illustration of a metal particle in an electrical field. The incoming electrical field will displace the conduction electrons, effectively separating the charges. Due to the curvature of the particle the electrons will be pulled on by the positive charges left behind. This leads to a restoring force, resulting in a resonance oscillation.

LSPR can be excited by direct light illumination, making it interesting for several branches in natural science, especially optical sensing solar absorption.

2.3.1 Quasi Static Approximation

The simplest way to investigate the interaction between a particle and the electric field is by utilising the quasi static approximation (QSA). This requires that the particle diameter is much smaller than the wavelength of the incoming light, i.e. $D \ll \lambda$. In this case an harmonically oscillating electromagnetic field can be seen as constant, with respect to gradients, over the particle. That means one can look at the simplified problem of a particle in an electrostatic field. One can then add the harmonic time dependence when the field distributions are known. The resonance condition derived for an homogeneous, isotropic sphere with radius a ($a \ll \lambda$) placed in the origin of a uniform static electric field $\boldsymbol{E} = E_0 \hat{\boldsymbol{z}}$ provides the fundamental theory for QSA, the sphere is illustrated in Figure 2.3.
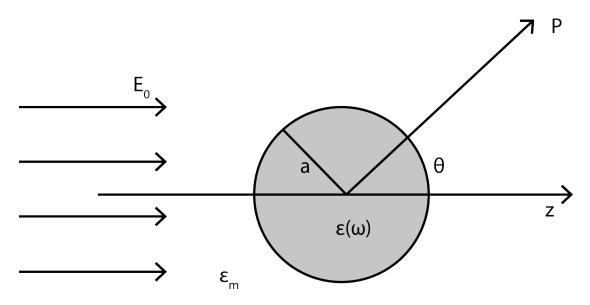
FIGURE 2.3: Homogeneous sphere placed in a uniform static electric field.

ϵ_m is the dielectric function for the surrounding medium, which is isotropic and non absorbing. The sphere's permittivity is described by $\epsilon(\omega)$. The electric field inside and outside of the sphere is found by solving Laplace equation [39]

$$\boldsymbol{\nabla}^2 \boldsymbol{\Psi} = 0 \tag{2.17}$$

with

$$\boldsymbol{E} = -\boldsymbol{\nabla}\boldsymbol{\Psi} \ , \tag{2.18}$$

where $\boldsymbol{\Psi}$ is the electrostatic potential. Due to azimuthal symmetry the potentials are independent of ϕ. The general solution is then [25]

$$\boldsymbol{\Psi}(r,\theta) = \sum_{l=0}^{\infty}[A_l r^l + B_l r^{-(l+1)}]P_l(cos\theta) \ , \tag{2.19}$$

where $P_l(cos\theta)$ are the Legendre Polynomials of order l. θ is the angle between the position vector $\boldsymbol{r}$ at point P and the z-axis [25]. The electric potentials has to stay finite at the origin, giving us the following solutions for the potentials $\boldsymbol{\Psi}_{in}$ on the inside and $\boldsymbol{\Psi}_{out}$ on the outside of the sphere [25].

$$\boldsymbol{\Psi}_{in}(r,\theta) \ = \ \sum_{l=0}^{\infty} A_l r^l P_l(cos\theta) \tag{2.20}$$

$$\boldsymbol{\Psi}_{out}(r,\theta) \ = \ \sum_{l=0}^{\infty}[B_l r^l + C_l r^{-(l+1)}]P_l(cos\theta) \ . \tag{2.21}$$

A_l, B_l and C_l are constants that can be determined by applying boundary conditions, giving us an unique solution for the electrostatic potential. The boundary conditions at $r \to \infty$ requires that $\boldsymbol{\Psi}_{out} \to -E_0 z = -E_0 r cos\theta$ and gives $B_1 = -E_0$ and $B_l = 0$ for

$l \neq 1$ [25]. A_l and C_l are determined at r = a. Here the boundary conditions are [25]

$$-\frac{1}{a}\frac{\partial \mathbf{\Psi}_{in}}{\partial \theta}\Big|_{r=a} = -\frac{1}{a}\frac{\partial \mathbf{\Psi}_{out}}{\partial \theta}\Big|_{r=a} \ , \tag{2.22}$$

$$-\epsilon_0\epsilon\frac{1}{a}\frac{\partial \mathbf{\Psi}_{in}}{\partial r}\Big|_{r=a} = -\epsilon_0\epsilon_m\frac{1}{a}\frac{\partial \mathbf{\Psi}_{out}}{\partial r}\Big|_{r=a} \ . \tag{2.23}$$

Due to equality of the tangential components of the electrical field and equality of the normal components of the displacement field, respectively. Hence $A_l = C_l = 0$ for $l \neq 0$, resulting in the following potentials [25]

$$\Psi_{in} = -\frac{3\epsilon_m}{\epsilon + 2\epsilon_m}E_0 r cos\theta \ , \tag{2.24}$$

$$\Psi_{out} = -E_0 r cos\theta + \frac{\epsilon - \epsilon_m}{\epsilon + 2\epsilon_m}E_0 a^3 \frac{cos\theta}{r^2} = -E_0 r cos\theta + \frac{\boldsymbol{p}\cdot\boldsymbol{r}}{4\pi\epsilon_0\epsilon_m r^3} \ , \tag{2.25}$$

where

$$\boldsymbol{p} = 3\pi\epsilon_0\epsilon_m a^3 \frac{\epsilon - \epsilon_m}{\epsilon + 2\epsilon_m}\boldsymbol{E_0} \ , \tag{2.26}$$

$\boldsymbol{p}$ is the dipole moment and $\boldsymbol{E_0}$ is the applied field. In other words, the applied field induces a dipole moment inside the sphere which is proportional to the magnitude of $|\boldsymbol{E}_0|$. The polarizability α, which is the capability of the sphere to be polarized by the electrical field, of the particles are related to the dipole moment by [25]

$$\boldsymbol{p} = \epsilon_0\epsilon_m\alpha\boldsymbol{E_0} \ . \tag{2.27}$$

By comparing equation (2.26) and equation (2.27) we get [25]

$$\alpha = 4\pi a^3 \frac{\epsilon - \epsilon_m}{\epsilon + 2\epsilon_m} \ . \tag{2.28}$$

This is the complex polarizability for a sphere of sub-wavelength diameter. The polarizability will be at its maximum, and experience a resonance enhancement, when the denominator in equation (2.28) goes to a minimum. When Im[ϵ] is small or slow-varying around the minimum, the resonance condition is given as [25]

$$\text{Re}[\epsilon(\omega)] = \epsilon_1(\omega) = -2\epsilon_m \ , \tag{2.29}$$

which is called the Fröhlich condition. Equation (2.29) indicates that the resonance frequency is strongly depending on the surrounding medium. One also sees that the resonance redshifts when ϵ_m increases. For a sphere, described by the Drude model, with air ($\epsilon_m \approx 1$) as its surrounding medium the Fröhlich condition is met at the frequency $\omega_0 = \omega_p/\sqrt{3}$. While for a sphere of Drude metal surrounded by water ($\epsilon_m \approx \sqrt{1.5}$) the Fröhlich criterion is met at $\omega_0 = \omega_p/2$ [29]. Thus, by adjusting the spectral shape of metal nanoparticles the LSPR is tunable [40]. The particle's electric fields can be derived by from equation (2.18) resulting in

$$\boldsymbol{E_{in}} = \frac{3\epsilon_m}{\epsilon + 2\epsilon_m}\boldsymbol{E_0} \tag{2.30}$$

$$\boldsymbol{E_{out}} = \boldsymbol{E_0} + \frac{3\boldsymbol{n}(\boldsymbol{n}\cdot\boldsymbol{p}) - \boldsymbol{p}}{4\pi\epsilon_0\epsilon_m}\frac{1}{r^3} \ . \tag{2.31}$$

As seen in equation (2.30) and equation (2.31) the resonance in α would lead to an resonance enhancement in the internal and dipolar field. It is this enhancement that is the foundation for many optical devices and sensors based on metal nanoparticles [25].

The preceding results are all based on electrostatics. In the following the electromagnetic fields radiated by a small particle at its plasmon resonance will be examined. For a sphere with radius a $\ll \lambda$ the dipole representation can be looked at in the light of the quasi-static approximation. Illuminated by an electric field, $\boldsymbol{E}(\boldsymbol{r}, t) = \boldsymbol{E}_0 e^{-i\omega t}$, the field will induce an oscillating dipole moment, with the polarizability described by equation (2.28). This results in scattering of the plane wave, where the following radiation can be characterized by a point dipole [25]. As the metal sphere can be described as an ideal dipole, it will scatter and absorb incoming light. This scattering and absorption will be greatly enhanced when the Fröhlich condition is fulfilled. Scattering and absorption is quantified by their respective cross sections, i.e. the probability that scattering or absorption of light will be caused by the particle. The cross sections are calculated via the Poynting-vector to [25]

$$C_{\text{sca}} = \frac{k^4}{6\pi}|\alpha|^2 = \frac{8\pi}{3}k^4 a^6 \mid \frac{\epsilon - \epsilon_m}{\epsilon + 2\epsilon_m} \mid^2 \tag{2.32}$$

$$C_{\text{abs}} = k\text{Im}[\alpha] = 4\pi k a^3 \text{Im}[\frac{\epsilon - \epsilon_m}{\epsilon + 2\epsilon_m}] \ . \tag{2.33}$$

Where $k = 2\pi/\lambda$ is the wave number, $|\alpha|$ the polarizability modulus and $\text{Im}[\alpha]$ the imaginary component of the polarizability. Once again it is clear that an resonance enhancement is achieved when the Fröhlich condition is met, i.e. at the dipole plasmon resonance [25]. Scattering scales with a^6 while absorption scales with a^3, meaning that for small particles ($a \ll \lambda$) absorption would dominate while for larger particles scattering takes over. Explaining why MNPs exhibit characteristic size-dependent colours in reflected light, e.g. as seen in the Lycurgus cup [25].

For a sphere with volume V in the quasi static limit with dielectric function $\epsilon = \epsilon_1 + i\epsilon_2$ the extinction cross section can be calculated as $C_{\text{ext}} = C_{\text{sca}} + C_{\text{abs}}$ [25]

$$C_{\text{ext}} = 9\frac{\omega}{c}\epsilon_m^{3/2}V\frac{\epsilon_2}{[\epsilon_1 + 2\epsilon_m]^2 + \epsilon_2^2} \ , \tag{2.34}$$

where c is the speed of light. The extinction cross section is dominated by absorption for small particles, while for particles larger than 100 nm scattering dominates [41]. The current results are obtained for a spherical nanoparticle, however it still gives a valid description of the physics behind localized surface plasmons for a sub-wavelength nanoparticle. Nonetheless, the quasi static approximation can be expanded quite easily to include elipsoids, and the special cases oblate and prolate spheroids. This is done by introducing a geometrical factor L_i to the polarizability α_i, where i represents the principal axes (i =1, 2, 3). For oblate and prolate spheroids this correction introduce two spectrally separated plasmon resonances, due to oscillations along the major and minor axes [25]. The oscillations along the major axis redshifts the resonance compared to a sphere with the same volume. Thus, the localized surface plasmon resonance can not only be tuned by the surrounding medium, but also by changing the aspect ratio of the particle [25].

As a general limit the quasi static approximation is valid for particles with diameters $D < 100$ nm [25]. In this thesis particles with diameters varying from 30 nm to 200 nm will be discussed. Thus, most of the particles will be well within the theoretical model

although some will lie above the maximum value. Langhammer et al. [41] found that the electrostatic model can successfully describe the energy dependence of the dipolar resonance, the full width at half maximum, and the total extinction cross section when $100 < D < 500$ nm. In this thesis we are primarily interested in the resonance and the cross section, therefore with these limitations in mind we will apply the electrostatic model.

2.3.2 Mie Theory

As mentioned previously the quasi static approximation is not valid for particles with diameter $D > 100$ nm. This is because for larger particles, $D \approx \lambda$, the particle will experience a significant phase change due to the drive field. Thus, the electrostatic approximation breaks down and an electrodynamic approach is required. In 1908 Mie [33] developed a complete theory on the scattering and absorption of electromagnetic radiation by a sphere. The optical properties of the particles in this thesis can all be described by the quasi static approximation. However, Mie theory describes important details to the LSPR that is not included in the electrostatic model. Such as, it predicts a redshift in LSPR with increasing particle size [25]. Intuitively this redshift can be attributed to the increased distance between the conduction electrons and the ion cores within the particle. Thus, leading to a smaller restoring force and therefore a lowered resonance wavelength [25]. In addition, the theory shows the importance of higher-order resonances as the particle grows larger, leading to a breakdown in the theory of conduction electrons being described as one collective motion. These higher order resonances can be excited by different frequencies of the incident electromagnetic radiation [38].

2.4 Spectroscopy

Spectroscopy is the study of the interaction between electromagnetic radiation and matter. When electromagnetic radiation is incident on matter the interactions can be divided into three categories; reflectance, absorption and transmittance. Reflectance (R) is defined to be the ratio of the reflected power (or flux) to incident power (or flux), as seen in equation (2.35) [42]. Transmittance (T) on the other hand is defined as the ratio of the transmitted power to the incident power and is given by equation (2.36) [42]. Lastly, absorption is when matter partially/fully absorbs the incoming radiation (photons) and converts it into thermal energy. Absorption is found through energy conversion as seen in equation (2.37).

$$R(\lambda) \equiv \frac{I_r(\lambda)}{I_i(\lambda)} \,, \tag{2.35}$$

$$T(\lambda) \equiv \frac{I_t(\lambda)cos(\theta_t)}{I_i(\lambda)cos(\theta_i)} \,, \tag{2.36}$$

$$1 = R(\lambda) + T(\lambda) + A(\lambda) \,. \tag{2.37}$$

I_r is the power/flux reflected back by the sample, I_i is the incident power/flux radiated on to the sample, I_t is the transmitted power/flux through the sample, while θ_t and θ_i are the angle of transmission and incident angle respectively.

For optical characterisation and analyses an integrating sphere set-up was used. The setup is explained in detail in Section 3.6, however a brief description will be given here. The setup consists of two spheres, a transmission sphere and a reflection sphere.

Therefore, the transmittance and reflectance could be measured individually and used to calculate the absorption of the MNPs. Another important optical property of MNPs is the extinction, which says how the intensity of the incoming light is reduced as it travels through matter. Extinction is the combined effect of the absorption in the particle and the scattering in all directions by the particle, as seen in equation (2.38) [43]. Scattering is when the incoming light is redirected by the particle without any other properties (e.g. frequency and polarization) being altered[42].

$$E(\lambda) \; = \; A(\lambda) \; + \; S(\lambda) \tag{2.38}$$

where A is the absorption and S is the scattering.

The following equation is used to find the reflectance of the MNP arrays placed in the integrating spheres

$$R(\lambda) = R_{\text{Sphere}}(\lambda) \frac{I_{\text{SR}}(\lambda) - I_{\text{SDark}}(\lambda)}{I_{\text{StdR}}(\lambda) - I_{\text{StdDark}}(\lambda)} \; . \tag{2.39}$$

R_{Sphere} is the reflectance of the spheres coating and is given as 0.98, $I_{\text{SR}}(\lambda)$ is the intensity of light reflected by the sample with I_{SDark} as the corresponding dark spectrum (light source blocked). $I_{\text{StdR}}(\lambda)$ is the intensity reflected by an reference standard, which is a standard coated with the sphere material. I_{StdDark} is the intensity of the dark spectrum for the reference standard.

For arrays measured in the integrating spheres the transmittance is calculated as

$$T(\lambda) = \frac{I_{\text{ST}}(\lambda) - I_{\text{STDark}}(\lambda)}{I_{\text{StdT}}(\lambda) - I_{\text{StdTDark}}(\lambda)} \; . \tag{2.40}$$

$I_{\text{ST}}(\lambda)$ is the intensity of the light transmitted by the sample and $I_{\text{STDark}}(\lambda)$ is the corresponding dark spectrum. $I_{\text{StdT}}(\lambda)$ is the transmitted intensity for an empty sphere and $I_{\text{StdDark}}(\lambda)$ is the dark spectrum of an empty sphere. The measurement process for transmittance and reflectance is explained in Section 4.2.2. An important concept for describing the properties of an optical material is the extinction coefficient, which is defined as [43]

$$\alpha_{\text{ext}}(\lambda) = f(C_{\text{abs}}(\lambda) + C_{\text{sca}}(\lambda)) = f(C_{\text{ext}}(\lambda)) \; . \tag{2.41}$$

Where f is the number of particles per unit volume and C is the different cross sections associated with absorption, scattering and extinction respectively. These cross sections are for single particles, in other words, the sample can modelled as the optical response for one particle multiplied with the concentration. For particles placed on a thin transparent substrate the extinction can derived from Beer Lambert's law [44] and the result is [45][46]

$$\text{Extinction} = \; \text{Absorbance} = -\log(\text{Transmittance}) \; . \tag{2.42}$$

Absorbance is the attenuation of transmitted radiant power, not to be confused with absorption which is the physical process of absorbing light [42]. The extinction spectra in this thesis are calculated with equation (2.42). To get the absolute extinction from the MNPs the extinction contribution from the substrate was subtracted as seen in equation (2.43)

$$\text{Extinction}_{\text{MNPs}} = \text{Extinction}_{\text{sample}} - \text{Extinction}_{\text{glass}} \tag{2.43}$$

Where the extinction of the glass was found through measurements of a unused glass substrate (no coating or particles).

2.5 Numerical Calculations

Mie theory is the only exact solution to Maxwell's equations. However, the theory is based on a single particle and cannot describe the optical properties of particle arrays or particle interactions. Numerical methods have been derived to try and solve these problems within realistic boundary conditions. Several different techniques which aim to solve Maxwell's equations exists, however they are all based on different assumptions and boundary condition.

2.5.1 Effective Medium Theory

Effective medium theory (EMT) describes macroscopic features of composite materials. General speaking, EMT is a description of a medium based on averages of its components derived from calculations. There are several different models utilizing this method, including the Maxwell-Garnett Approximation and Bruggerman's model. Maxwell-Garnett is an electrostatic theory, and the foundation is laid out in Section 2.2. This theory can be used on an array of particles, as presented in this thesis. However, an adjustment to equation (2.14) has to be made to account for the average volume of the particles in the array.

2.5.2 Discrete Dipole Approximation

Discrete dipole approximation (DDA) calculates scattering and absorption of electromagnetic waves by particles of arbitrary shape and composition [47]. There are two ways of deriving DDA, the physical clearer way is to replace the particles/scatterer with a set of point dipoles. Which in turn will interact with each other and the electrical field, giving rise to a set of linear equations. This set can then be solved with regards to the polarization, and all the information about the scattering can be found from the polarizations [47]. The other way, which gives a better mathematical insight to the approximation, is to solve the integral equation for the electric field. Which is done by dividing the scatterer into small cubical subvolumes [47].

2.5.3 GranFilm

GranFilm is a software developed by Simonsen and Lazzari which models a solution to the Maxwell equations based on the Bedeaux-Vlieger model [48]. This is an electrostatic model that describes the far-field optical properties of MNPs supported on a substrate. The transmittance of the MNP is found by solving Laplace equation by a multipolar expansion of the electrostatic field [48]. In the model, the particles are approximated as either spheroids or spheres truncated by the substrate. The plan was to use GranFilm for theoretical simulations in this thesis, as the software is free and available. In additions is has been used in previous thesis with success. Unfortunately due to time limitations the theoretical solutions could not be implemented in this work.

2.6   Absorbing Array

The goal of this thesis is to develop a solar absorber based on metal nanoparticles utilising LSPR. In other words an array which would absorb all wavelengths of light that reaches the Earth's surface from the sun. To achieve this an optimum composition of the MNPs has to be devised. The extinction spectrum has two contributors as shown in equation (2.38), absorption and scattering. A perfect solar absorber would have its extinction spectrum dominated by absorption with no contribution from scattering, this would ensures that no energy is lost to reradiation/transmission processes. Hence it is important to utilise particles and particle structures which is dominated by absorption and not scattering. Therefore, working within the boundaries of the quasi static approximation and Mie theory an optimum composition of particles is to be found. From the quasi static approximation, see Section 2.3.1, absorption dominates for particles with a diameter sub 100 nm. Meaning that the broad spectrum absorber should contain particles within this range to maximum the absorption efficiency. As absorption scales with a^3 (where a is the radius of the particle), larger particles would dominate over the smaller ones, making it especially hard to measure the contribution from the smaller ones. The extinction efficiency is the ratio between the extinction cross section, as seen in equation (2.34) , and the geometrical cross section [37]. Where the correlation between extinction efficiency and the extinction is given as

$$\text{Exctinction efficiency} = \frac{C_{\text{ext}}}{C_{\text{geo}}} = \frac{\text{Extinciton}}{\text{Surface coverage}} \ . \tag{2.44}$$

Where surface coverage is the total area which the particles cover, C_{ext} is the extinction cross section and C_{geo} is the geometrical cross section of the particle. Thus, one would need either a high extinction efficiency or a high surface coverage to achieve complete interaction with the incident photons. Utilising MNPs provides an upper limit to the surface coverage as particles will start to couple if placed too close to each other. Hence, it would be important to have particles with a high extinction efficiency to reach the extinction goal.

Chapter 3

Experimental Equipment

The current chapter presents the experimental equipment used to produce the MNP arrays, as well as the equipment used to characterise the optical and physical properties of the MNPs. It starts with a thoroughly discussion of the electron beam lithography and scanning electron microscopy system, followed by a description of the metal deposition system, the thin film analyser and the integrating sphere setup. The experimental procedure is described in Chapter 4.

3.1 Lab Facilities

All of the experimental procedures were done at UiB's nanostructure laboratory, with the exception of the integrated spheres. The nanostructure laboratory is located at the Institute of Physics and Technology, and consists of five main rooms; Entrance Area, ISO 7 standardised cleanroom cabinet, storage room, semi-cleanroom and a ISO 5 standardised cleanroom. The ISO standards for cleanrooms are based on the maximum amount of particles larger than 0.1 µm per cubic meter allowed in the room. For example, the ISO 5 cleanroom allows a maximum of 10^5 particles per m^3, while normal outdoor air is classified as ISO 9 [49]. The contamination in the cleanrooms is controlled by a laminar flow of pressurized and temperature controlled air. This creates a positive pressure, forcing airborne dust out through integrated gaps at floor level. In addition all staff have to follow a dress code to limit the introduction of contaminating particles. The equipment requires a varying degree of cleanliness, hence it is placed in different rooms within the laboratory. Sample preparation requires the lowest level of contamination, thus the fume hood, spin coater and hot plate is placed in the ISO 5 clean room. The electron beam evaporator is located in the semi clean room, while the ISO 7 cleanroom cabinet contains the electron beam lithography system.

3.2 Electron Beam Lithography

Electron beam lithography (EBL) is the process of scanning a highly focused electron beam across a substrate coated in an electron sensitive material, the material is termed a resist. The physical and or chemical properties of the resist will be changed when exposed to electrons, hence a pattern can be developed. Resist interactions are further explained in Section 3.3.1 and the developing steps are discussed in Chapter 4. The advantage of EBL compared to other lithography techniques is that it can create arbitrary patterns without using masks. This is an advantage as the mask will act as slits, resulting in a diffraction limit to the final resolution. Therefore, EBL can create patterns with high resolution (sub 10 nm), high density, high sensitivity and high reliability [50]. However, since masks are not used the beam has to be moved around on the sample to expose the targeted areas instead of an instant exposure of the mask. Thus, longer write times

are needed for EBL, limiting its use to smaller arrays and research where resolution is of high importance.

3.2.1   Raith e_Line Electron Beam Lithography system

The electron beam lithography (EBL) system at UiB's nanostructure laboratory is a SEM outfitted with a beam blanker, high precision laser interferometer controlled sample stage and a pattern generator. The system is depicted in Figure 3.1 and schematically illustrated in Figure 3.2.
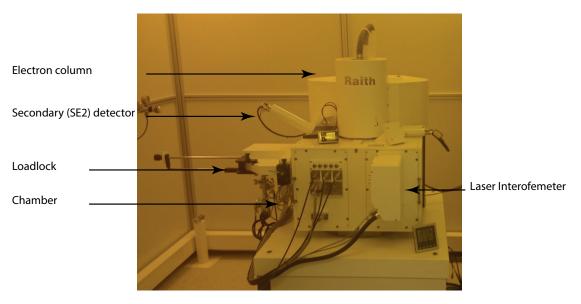
FIGURE 3.1: The electron beam lithography system at UiB's nanostructure laboratory. The high-speed patterning computer system is not depicted.

The electrons are emitted from a thermal field emission gun in the electron column. Thereafter they are accelerated through the column by an acceleration voltage, where the maximum voltage for this system is 30 kV. To control the width of the electron beam it is sent through the aperture, which is simply a hole of adjustable size. The system has six different apertures in the range of 7.5 μm to 120 μm. The beam is then focused onto the sample surface by electromagnetic lenses, where the beam position is controlled by scanning coils and moved with respect to the sample surface. To allow for a quick transition between sample exposure and non-exposure an electrostatic deflector is used as a beam blanker, making it possible to blank the beam without tuning off the beam whenever non-exposure is required. The system is equipped with two detectors to create a image of the sample, one InLens detector and one secondary electron (SE2) detector (The different resist-electron interactions will be explained in Section 3.3). The InLens detector is mounted in the final lens and collects SE1 with a higher efficiency compared to the SE2 detector, as only electrons directly emitted from the sample volume (SE1 and SE2) is collected. It can also discriminate against the SE3 electrons (background noise), decreasing the signal to noise ratio. Therefore, it has a higher surface sensitivity compared to ordinary SE detectors. For the SE2 detector we use a 300 V collection bias, to attract low energy SEs created by backscattered electrons. The SE2 detector is mounted with an angle to the sample surface, illustrated in Figure 3.2, making it possible to extract topographic information using this detector. In plain English EBL is based on

bombarding the sample with electrons, then extracting ionised and scattered electrons to create an image of the surface. When writing a pattern the amount of electrons hitting the surface will greatly influence the end results. Therefore, it is important to control the amount of electrons per area reaching the surface. This is done through exposure dose calculations, where the exposure dose is the amount of electrons hitting the sample surface per area. It is divided into three categories: area dose, line dose and dot dose. Which is calculated from the beam current, dwell time and step size. The formulas for 2 dimensional (areas) structures, 1 dimensional (lines) or 0 dimensional (points or dots) are as follows

$$\text{Area dose } [\mu C/cm^2] \quad = \quad \frac{\text{Dwell time [ms]} \ \times \ \text{Beam current [nA]}}{\text{Step size}^2 \ [cm^2]} \ , \qquad (3.1)$$

$$\text{Line dose } [pC/cm] \quad = \quad \frac{\text{Dwell time [ms]} \ \times \ \text{Beam current [nA]}}{\text{Step size [cm]}} \ , \qquad (3.2)$$

$$\text{Dot dose } [pC] \quad = \quad \text{Dwell time [ms]} \ \times \ \text{Beam current [nA]} \ . \qquad (3.3)$$

The dwell time is defined as the time the beam exposes each point, beam current depends on the aperture and acceleration voltage used when writing. The step size is the smallest step the stage or beam can be moved. Patterning and the effect of the exposure dose will be explained in more detail in Section 3.3.

If the sample surface is an insulating material (e.g. borosilicate glass) electrons would accumulate on the surface causing a considerable drift in the electron beam which could lead to pattern distortions in the EBL process or image distortions in the SEM process. To avoid this charging effect non-conductive samples must be coated with a conductive layer (e.g. gold/palladium or chromium). Since the EBL system does not utilise predetermined masks, patterns can be created in the CAD (Computer Aided Design) software which is integrated in the Raith e_Line system, or files of the ASCII (American Standard Code for Information Interchange) format can be imported. These patterns will function as a map for the electron beam, ensuring that the correct areas are exposed. The size of the CAD file represents the area which the system would write by deflecting the beam, that is without having to move the stage. This means that if the CAD file area is too large a reduction in the resolution will be experienced. To avoid this drop in resolution, the pattern can be divided into several smaller segments called writefields (in this thesis they are 100 μm × 100 μm). Neighbouring writefields are stitched together by moving the sample stage with nanometre precision. Alternatively the entire process can be done in FBMS (Fixed Beam Moving Stage), but this has writing restrictions and can only write continuous areas, lines and circles.
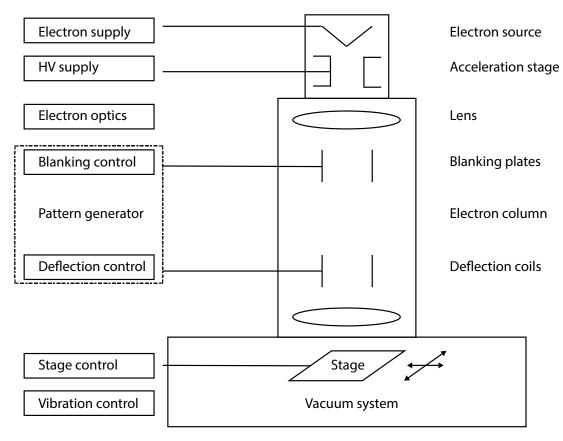
FIGURE 3.2: Schematic of the essential parts of the EBL system. Re-drawn from [50].

3.3 Electron Beam and Resist Interactions

When the electron beam is scanned over the sample surface, electrons will penetrate into the sample and interact with their surroundings. This will start a series of low-energy elastic collisions slightly deflecting the incident electrons, and is called forward scattering. Forward scattering leads to a broadening of the electron beam exposure, and thus reduces the final resolution. As the electrons penetrate deeper into the substrate there is a high probability that they will undergo large angle collisions and eventually re-emerge at some distant point in the resist. This is known as backscattered electrons and they can lead to what is called the proximity effect. This effect can lead to increased exposure at neighbouring structure, resulting in overexposure and pattern distortion [50]. However, the main contributor to the exposure dose is the secondary electrons created as ionization products when the primary electrons interact with the substrate.

3.3.1 Resist

In this thesis PMMA (Poly(methyl methacrylate)) is used as the resist, which is a long-chain polymer commonly known as plexi glass. When a long chain polymer is exposed to electrons the incident electron beam will break down the long chain polymer into smaller, more soluble fragments. Resists which becomes more soluble during electron beam exposure is termed positive resists. A negative resist on the other hand would be a short chain polymer. In that case a cross linking would occur when the polymer is exposed to a electron beam, this cross linking would bind smaller polymers together and make the area

exposed less soluble. The solubility of the resist is a key factor during the development procedure explained in Chapter 4. Resists can be used in single-layer schemes or several resists can be used together to form multi-layer schemes. The advantage of utilising a multi-layer scheme is that the final resolution can be increased without altering the EBL writing parameters, hence a multi-layer design would be preferable when very small structures are created. For the work done in this thesis a single layer scheme and a bi layer scheme was employed. The two different resist schemes are illustrated in Figure 3.3.
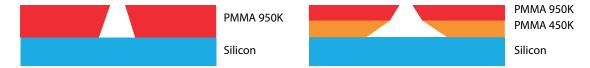
FIGURE 3.3: A sketch showcasing the wanted undercut profile for a single layer scheme (left) and a bi-layer scheme (right). The undercut prevents the metal from creating a continuous layer during the deposition.

In a bi-layer design it is important that the underlying resist is more sensitive than the top one, creating a larger undercut when exposed to the electron beam. The undercut profile ensures that when metal is deposited after development a discontinuous layer is created. In other words, the metal is not deposited on the side walls of the resist. Development is usually performed by immersing the sample in a liquid developer. For a positive resist this will dissolve the scissored fragments, while for a negative resist the non-crosslinked chains are dispersed. Temperature and time would influence the final resolution, therefore it is important to keep these constant to avoid varying results.

3.3.2 Substrate

The optical properties (e.g. reflection, transmission and absorption) of the manufactured MNP arrays is important as the design for a solar absorber based on MNPs is the aim for this work. Therefore, the particles were created on Borosilicate glass coverslips (No. 1 coverslips Thermo Scientific), which is transparent to visible light and ideal for optical characterisation. However, glass is non-conductive making it a far from ideal substrate for SEM imaging or EBL writing as they prefer a conductive surface to prevent surface-charging effects. Hence, a conductive layer (e.g. chromium or gold-palladium) above or below the resist is required to avoid charge accumulation.

3.4 Electron Beam Evaporator

At the UiB Nanostructure Laboratory an electron beam evaporator is used to deposit thin films. The installed instrument is a Temescal FC 2000, which is depicted in Figure 3.4, and the evaporation process is controlled by the Temescal Control Computer Software (TCS). Within the TCS several recipes for each of the available metals is stored, and the recipes can be altered between evaporation to ensure the wanted result. Rate of deposition, deposition thickness and angle of deposition are among the variables that can be adjusted by the user. At the current time gold, nickel, aluminium, titanium, chromium and silicon oxide are the accessible metals in the electron beam evaporator. The metals are stored in separate crucibles created to withstand the immense temperature during evaporation. After configuration of the recipe the deposition

chamber has to be pumped to a high pressure (minimum 2 nbar) before the evapora-
tion process can begin. This is done to ensure that the mean free path (the average
distance an atom/molecule can travel without colliding with another particle) of the
evaporated atoms/molecules are longer than the distance from the evaporation material
to the substrate. The electron source is placed beneath the evaporation material to avoid
contamination of the electron gun. A 10 kV (CV-12SLX) voltage is used to accelerate
the electron beam and permanent magnets are used to guide the electron beam onto
the material to be evaporated. When hit by the electrons the material will start to heat
up before it eventually will begin to evaporate. There are two shutters installed in the
deposition chamber, when the first one is opened the evaporated material will deposit
on a quarts crystal within the chamber. As the material deposits on the crystal the res-
onance frequency will change, the computer software can then calculate the deposition
rate. Finally, when the deposition rate is calculated the second shutter opens and the
substrate is exposed to the material vapour.

FIGURE 3.4: The electron beam evaporation system located in the UiB
nanostructure laboratory.

3.5 Thin Film Analyser

For thin film thickness measurements the UiB nanostructure laboratory has a Filmetrics-
F10-RT measurement instrument, which is depicted in Fig 3.5. A tungsten halogen light
source illuminates the sample, and the reflected and transmitted light is then collected
by two VIS-NIR grating spectrometers (spectral range 380 nm to 1050 nm). These
spectrometers are connected to a computer and controlled by the FilmMeasure software
which can calculate the thickness based on these spectra. The nominal thickness and
material of the sample is given by the user prior to the measurements. The FilmMeasure
software finds the thickness by analysing the collected reflectance and transmittance

spectra. These data are then compared to a series of calculated spectra. To evaluate the compliance between the measured data and calculated data a goodness of fit (GOF) is used, that is a number between 0 and 1 is given. Here 1 is a perfect match and 0 is a mismatch, values above 0.95 is acceptable. In this thesis the thin film analyser was mainly used to determine the thickness of the PMMA resist.

FIGURE 3.5: The thin film analyser located in UiBs nanostructure laboratory.

3.6 Integrating Sphere

The thin film analyser could measure the transmittance/reflection spectra of the sample, although only the light directly transmitted/reflected through/off the sample is collected. This provides a challenge as the MNPs are expected to absorb light, which will contribute to the total extinction. Due to a small acceptance angle in the optical fibre the thin film analyser can not detect this loss in intensity. Therefore, an integrated sphere setup was implemented as it can collect light scattered in all spatial directions. The setup is illustrated in Figure 3.6 and depicted in Figure 4.5. In all simplicity an integrated sphere can be viewed as a spherical cavity coated with an ideal diffusely reflecting material. Light emitted into the sphere will be scattered in all spatial directions by the sphere walls, hence the light inside the sphere is uniform. In other words any spatial, angular or polarization variations from the light source are lost. As mentioned earlier the integrated sphere collects light scattered in all spatial directions. Thus, it is capable of separating the contributions from absorption and scattering to the total extinction [41]. The amount of scattered light by the sample equals the sum of the total amount of light transmitted through the sample and the total amount of light reflected by the sample. For larger spheres a baffle is integrated within the sphere. The baffle prevents collection of light directly from the light source. In the case of smaller sphere, as those

employed in this work, a baffle is not needed due to the small radii of the spheres in combination with the low acceptance angle of the optical fibre [49]. Due to the design of the integrating sphere there are a mainly two sources of error. Firstly the sample, detector and entrance ports are not coated with the highly reflecting material thus the light hitting the ports is not scattered in all directions. Secondly, some light will escape out of the ports and information is lost. Carr et al. discovered that the total area of ports should not exceed 5% of the internal surface of the sphere [29]. The setup consists of two spheres, one which measures the transmitted light through the sample and one which measures the light reflected of the sample. The transmission sphere (Ocean Optics ISP-50-8-I) and the reflection sphere (Ocean Optics ISP-50-8-R-GT) has an internal diameter of 50 mm and a sample port with a diameter of 8 mm. The spectral range of the spheres is 200 nm - 2500 nm due to the reflective coating. The reflection sphere is fitted with a gloss trap, which is a light trap used to exclude the specular contribution of the reflected light (although, not relevant in this thesis work). The light entrance port is mounted in the reflection sphere at an 8° angle with respect to the sample surface, while the gloss trap is fitted at an -8° angle. In the wavelength range of 400 nm -1500 nm the reflectivity of the highly reflective coating is greater than 98 % and greater than 95 % in the range 250 nm - 2500 nm. A tungsten halogen light source (Ocean Optics HL-2000) with a wavelength of 360 nm - 2400 nm was used. The size of the beam at the sample port (spot size) was found to be approximately 3 mm [29]. To guide the light through the setup optical fibres (Ocean Optics P400-2-VIS-NIR) are employed. The optical fibres have a diameter of 400 µm and a spectral range of 400 nm - 2100 nm. The employed spectrometer (Ocean Optics USB400-VIS-NIR ES) has a spectral range of 350 nm - 1000 nm and employs an entrance slit of 25 µm.
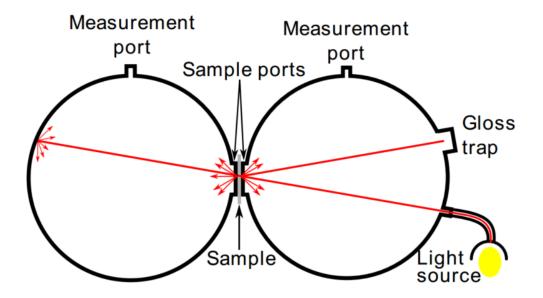
FIGURE 3.6: Illustration of the integrated sphere setup.

Chapter 4

Experimental Procedure

This chapter contains a walkthrough of the experimental procedures used in this thesis to produce a solar absorber based on MNPs. The procedure of creating large arrays of MNPs by the means of EBL was developed and refined by Håvardstun [38] and Flatabø [29] respectively. The process was further developed in regards of creating an array consisting of more than one metal and several varying particle sizes.

4.1 Sample Preparation

The fabrication of the MNP arrays consists of several steps, each one influencing the resolution and end result. Therefore, an optimized procedure is important to achieve consistent and good results. This optimization has already been done by Håvardstun [38] and Flatabø [29] in their respective theses. Hence only a short presentation of the procedure will be given her.

4.1.1 Equipment Cleaning

Too avoid unnecessary contamination of the samples all the equipment (tweezers, containers, wafers etc.) has to be properly cleaned prior to use. This was achieved by using three solvents

1. Acetone (Emparta ACS, Merk KGaA)

2. Methanol (Emparta ACS, Merk KGaA)

3. 2-Propanol (Emparta ACS, Merk KGaA)

The equipment were rinsed with the solvents in the above order, then dried with nitrogen gas. In 2013 Håvardstun [38] discovered that it was possible to get enhanced adhesion if the glass wafers went through an additional cleaning process. Thus, prior to use the glass wafers were placed in an ultrasonic bath in acetone for 10 minutes, followed by 10 minutes in 2-Propanol.

4.1.2 Resist Coating

Due to the varied particle sizes sought after in this thesis, two different resist schemes were incorporated.
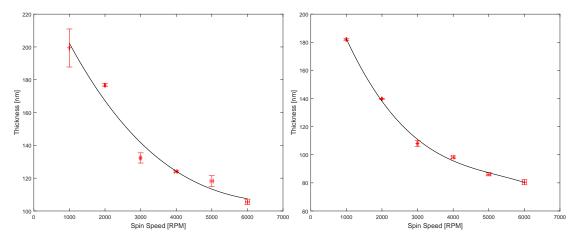
- PMMA 950K (Allresist AR-P 672.08) diluted in Anisole, ratio 2:3, was used in the single layer scheme

- PMMA 495K (Microchem 495K PMMA A8) diluted in Anisole, ratio 2:3 and PMMA 950K (Allresist AR-P 672.02) non-diluted were used in the bi-layer scheme.

To evenly spread the resist onto the glass substrate a spin coater (Chemat technology KW-4A) was used. The spin coating process can be divided into two processes, a slow spin stage and a fast spin stage. The slow speed stage disperses the liquid, while the high speed stage spreads it homogeneously across the wafer. Before resist was added to the sample it was placed on the sample holder (silicon wafer with sticky tape on it) inside the spin coater, a vacuum pump kept the sample holder in place during the coating procedure. With the help of a glass pipette the resist was added to the sample surface, roughly 3/4 of the wafer surface was covered. After the spin coating was completed the samples were soft baked on a hot plate (UniTemp GmbH – Eurotherm 2132) to harden the PMMA and evaporate residual solvent.
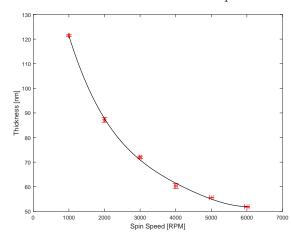
To make the lift-off process easier it was decided to utilise a thick layer of resist, that is a thickness in the range of 150 nm - 180 nm. The thickness of the resist for every substrate could be measured with the thin film analyser, however this is time consuming and as a result, resist thickness was plotted as a function of spin speed. These curves were created by measuring the thickness of the resist for several spin speeds (Rounds per minute (RPM)). The results are shown in Figure 4.1

For the single layer scheme the slow spin stage speed was set to 2000 RPM for 6 seconds and the high speed stage speed was set to 2250 RPM for 60 seconds. Obtaining a thickness of 160 nm $\pm$ 1 nm, as seen in Figure 4.1. Directly after being coated the sample was soft baked for 5 minutes at 175 °C.

The bi-layer scheme was made by first coating the sample with PMMA 495K, then the process was redone with undiluted PMMA 950K. PMMA 495K was coated on with the slow speed stage set to 500 RPM for 6 seconds and the high speed stage set to 6000 RPM, providing an end result of 80 nm $\pm$ 1 nm. The sample was then soft baked for 3 minutes at 175°C. The undiluted PMMA 950K utilised a slow speed stage at 500 RPM for 6 seconds and a high speed stage at 2000 RPM for 60 seconds. This resulted in a layer of 90 nm $\pm$ 1 nm. Straight after the coating process the sample was soft baked at 175°C for 6 minutes. The final thickness for the bi-layer scheme was 170 nm $\pm$ 2 nm.

(A) Resist thickness plotted as a function of spin speed for PMMA 950K.

(B) Resist thickness plotted as a function of spin speed for PMMA 495K.

(C) Resist thickness plotted as a function of spin speed for undiluted PMMA 950K.

FIGURE 4.1: PMMA thickness is plotted against the spin speed of the spin coater. 18 data points were used to create the fitted curve. The errorbars on the x-axis is 1 % of the RPM, while standard deviation is used to calculate the error in the measured thickness. Top left shows the diluted 950K PMMA, top right shows the diluted 495K PMMA while the bottom shows the undiluted 950K PMMA.
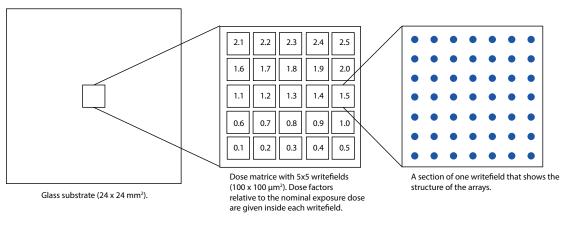
4.1.3 Conductive Layer

Due to the non-conductive nature of the glass substrates a thin conductive layer had to be coated on top of the resist prior to the EBL procedure. This was done to avoid charging effect and deflection of the electron beam during the e_Line writing procedure.

3 nm ± 1 nm of chromium was deposited on the samples with the electron beam evaporator (Temescal FC-2000). The deposition process is explained in Section 4.1.8.

4.1.4 Dose Matrices

Due to the complex interactions between the electron beam and the resist, establishing the correct exposure dose had to be done through several test matrices. These test matrices are termed dose matrices. Each dose matrices were on the size of one writefield (100 µm) and would contain a given set of particle sizes. Matrices of this size would not

require long writing times, therefore making it an efficient way to calculate the correct dose. An illustration of how the dose matrices were made is showed in Figure 4.2

Dose matrice with 5x5 writefields (100 x 100 μm²). Dose factors relative to the nominal exposure dose are given inside each writefield.

A section of one writefield that shows the structure of the arrays.

Glass substrate (24 x 24 mm²).

FIGURE 4.2: Schematic description of the preparation of dose matrices. Each square is given a different dose(multiple of the nominal dose). By going through each of the matrices it was possible to find the correct dose for every particle.

As a starting point the recommended dose was found in literature provided by the resist manufacturer, then the doses were varied around this nominal value. After developing the resist, metal deposition and lift-off the samples were analysed in the SEM. Going through each of the matrices, particle size and shape were analysed. When particles with the correct size and shape were found the dose factor was written down for further use in the large arrays. A different approach would be to have a constant dose through all the matrices, but vary the dimensions of the particles. This is called size matrices and similar to dose matrices they are used to find the correct dose and dimensions for the particles.

4.1.5 Full Scale Matrices

The glass substrate (i.e. glass wafer coated with PMMA and Chromium) was placed on the sample holder and locked in place using two clips. Before the loading procedure was initiated polystyrene beads were placed in each corner of the glass sample with the help of a toothpick. These would later on be used as focusing aids due to their well defined circular shape and known radius. With the sample holder allocated in the loading dock of the e_Line the loading procedure was initiated. After completing the loading procedure the voltage was turned on and appropriate aperture was chosen. In the single layer resist scheme the acceleration voltage was set to 10 kV and the aperture to 30 μm. The bi-layer scheme used an acceleration voltage of 20 kV, while the aperture was set to 20 μm for particles smaller than 55 nm and 30 μm for particles larger than 55 nm. This change in aperture was made to make it possible to recreate the smallest particles in the large arrays. With the help of the wafer map the electron beam was moved to the location of the polystyrene beads. These were then used to optimize the working distance (i.e. the distance between the final lens and the sample), aperture and stigmation. Aperture controls the electron current through adjustment of the beam diameter, while stigmation correction ensure that the focal length is equal in both x an y direction. Due to the thin substrate a tilt in the sample plan was present, leading to a varied working distance across the sample. Therefore, an automatic working distance

correction tool was enabled. The working distance was measured at three different locations on the sample, then the software could determine the true orientation of the tilted sample, with respect to the horizontal plane, and correct it. Thus, making sure optimum focus was achieved throughout the entire process. In addition the working distance was found at two diagonal opposite corners of the MNPs array. These were then averaged and used as the initial working distance for the writing. Following the optimisation process writefield alignments were done, this was completed to adjust the electromagnetic/electrostatic deflection system inside the column to the high precision stage. This ensured a complete overlap between the movement of the stage/beam and the coordinate system used. A suitable site for the writefield alignments would be any object with a distinct feature at around 1000 magnification, this could be either particle contamination (e.g. dust) or a build up of polystyrene beads. First the writefield alignments were done manually by dragging vectors from given positions to the chosen particle contamination, this was done at an increasing magnification. Secondly, an automatic writefield alignment were performed at very high magnification. In the automatic procedure a reference mark is scanned and stored, then several scans is completed and compared to the reference. The shifts are then calculated and the new alignment parameters are activated. High precision writefield alignments was mandatory to reduce stitching errors in the intersection between each writefield. On the sample holder there is a Faraday's cup (conductive cup), and on completion of the writefield alignment the beam was focused on the Faraday's cup and the beam current was measured. Afterwards the nominal dose was set and dwell time calculated. Then the CAD file containing the pattern was imported, given a starting location and dose factor (multiple of the nominal dose). Lastly the exposure was initiated.

4.1.6 Chromium Etching

The developer could not develop the sample through the chromium layer, therefore the chromium had to be etched away. This was done by placing the sample in a chromium etchant (Transene company inc.) for a few seconds. Thereon, the sample was thoroughly rinsed in deionized water followed by 2-propanol and in the end blown dry by pure nitrogen gas.

4.1.7 Development

For the development of the resist Entwickler (AR 600-56) mixed with IPA at the ratio 1:3 was used as the developer. The sample is immersed in the developer for 2 minutes before 2-propanol was used to stop the developing process, the sample was then rinsed in 2-propanol for 15 seconds. Lastly pure nitrogen gas was used to blow dry the sample.

4.1.8 Metal Deposition

A homogeneous thin metal layer was deposited with the electron beam evaporator (Temescal FC-2000). Four different sources of metal were used during this work:

- 3 nm Chrome

- 20 nm Aluminium

- 20 nm Gold

- 20 nm Nickel

Chrome was used as a conductive layer on the glass substrate to avoid charging during the writing of the MNP arrays. The first dose matrices was made on a silicon substrate, but to get the correct doses for glass substrates nickel nanoparticles were made due to the low material cost. The large arrays, produced to test the optical properties of the MNPs, were made with aluminium and gold. The main process chamber is held at high vacuum during standby to prevent contamination. Hence it was necessary to vent the chamber to ambient pressure before the samples could be loaded. After the venting the chamber could be opened and the sample holder removed. Thereupon, the samples were carefully mounted and held in place with clips before the sample holder was placed back on to the mount inside the process chamber. Deposition material, final thickness and angle of deposition were then selected in the Temescal software. The process chamber were then pumped back to high vacuum and the voltage turned on (CV-12SLX). When the automation process had completed, the process chamber was vented and the samples carefully removed from the sample holder. Lastly the chamber was pumped to high vacuum and the voltage turned off.

4.1.9   Lift-off

Removing the excess metal from the substrates was done by the process called lift-off. The samples would be immersed in N-Methyl-2-pyrrolidone (NMP) which would dissolve the PMMA beneath the metal layer, the excess metal could then be peeled of without damaging the MNPs. A petri dish was filled with enough NMP to fully cover the sample and then heated to 80°C on a hot plate (Stuart CB160). The temperature was closely monitored with a thermometer, as the boiling point of NMP is 90°C and the vapour is harmful. When 80°C was reached the sample was carefully, face up (side with PMMA and MNPs), lowered down into the solution. If everything had be done properly up to this point small cracks would immediately be seen on the surface. For the single layered PMMA sheets of the metal would start to loosen after 5 to 10 minutes, and after 15 minutes the metal layer was completely removed. When switching over to the double layer PMMA a longer lift-off time was needed. The metal layer would still crack after a few seconds and loose sheets would start to be seen after 10 to 15 minutes, but it would take 40 minutes before the entire layer was removed. Aluminium was found to have a longer lift-off time than gold, taking up to an hour before the excess metal was removed. Another difference as well was that the aluminium layer would crumble compared to the gold layer which would loosen as a whole layer. Instantly after the sample were taken out of the NMP bath it was carefully rinsed with 2-propanol and blow dried with nitrogen gas. Sometimes during the process small scratches along the edges of the samples were made to speed up the process. Disturbing the petri dish in any other way have in previous work shown indications of leading to a higher particle loss [29].

4.1.10   Mixed Metal Layers

To increase the efficiency of the MNP based solar absorber two or more materials can be used within the array to increase the spectral range in which light is absorbed. Therefore, an overlapping procedure was developed which allowed for both gold and aluminium particles within the same array. The overlapping procedure is simply put completing the previous mentioned sample preparation and writing procedure twice on the same wafer.

To help manoeuvring the sample surface and writefield placements the e_Line software utilizes two coordinate systems. First one is termed XY, which is the reference system and anchored to the wafer map. The second one is the UV coordinate system, this systems origo is defined by the user making it easy to navigate on the sample. The UV coordinates would be associated with the corresponding XY coordinates. During the first writing, in addition to the array pattern, global alignment marks were also implemented in the structure. These made it possible to align the coordinate system from the first writing to the coordinate system during the second writing. This was important since placing the sample in the exact same spot in the sample holder with nanometer precision was not possible. A global alignment mark was placed outside each of the four corners of the sample, far enough away to not interfere with the optical measurements at a later stage. Additionally some scaled down marks were placed around the alignment mark outside origo of the pattern. The UV coordinates of these marks were then written down for use during the second writing. The alignment marks are illustrated in Figure 4.3. The writing procedure and lift-off were then completed normally before a new layer of resist and chromium were coated on. Then the sample was mounted back on the e_Line sample holder and the loading procedure was completed. After setting origo and completing the optimization of focus, stigmation and aperture the new coordinate system was matched with the old system used during the first writing procedure. This was done by localizing the global alignment marks and using the 3-point alignment tool. The 3-point alignment tool made it possible to give XY coordinates specific UV coordinates and then adjust the UV coordinate system based on those 3 points. Thus, each of the global alignment marks were located and identified before given their original UV-coordinate. By performing this procedure it was ensured that the second layer of writefields were placed at the same location as the first layer.
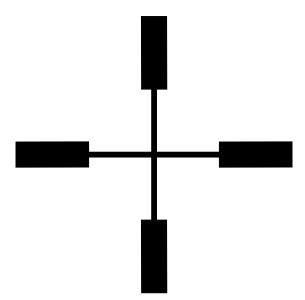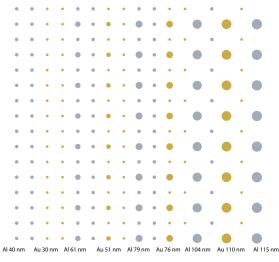
FIGURE 4.3: Illustration of the global alignment marks. These marks were placed outside every corner of the array and their UV-position were saved. In the event of an overlapping structure these marks could be used during the second writing process to align the old coordinate system with the new one. Ensuring the correct placement of the second layer of particles.

The 3-point alignment had to be done prior to the writefield alignment to ensure
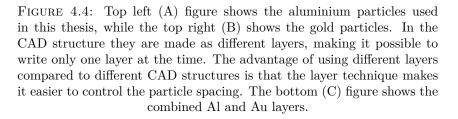
that the system was aligned to the correct coordinate system. Another concern during the overlap procedure was the fact that the writefields used had to fit within each other. This problem was solved by implementing the different layers the CAD structure offered. Placing particles in various layer within the same CAD structure enables the user to work on a specified amount of layers at a given time. In this case the gold and aluminium nanoparticles were placed in two different layers within the CAD structure, making it possible to create the wanted structure with ease. The CAD structure and layers used for the overlap procedure are illustrated in Figure 4.4.

(A) The aluminium layer in the CAD structure.

(B) The gold layer in the CAD structure.

(C) The combined layers in the CAD structure.

FIGURE 4.4: Top left (A) figure shows the aluminium particles used in this thesis, while the top right (B) shows the gold particles. In the CAD structure they are made as different layers, making it possible to write only one layer at the time. The advantage of using different layers compared to different CAD structures is that the layer technique makes it easier to control the particle spacing. The bottom (C) figure shows the combined Al and Au layers.

It was found experimentally that for the orgio of the two layers to coincide after the 3-point alignment, the second layer had to be shifted 1/4 of the writefield size in positive U and V direction. The theoretical reasoning for this was never found, but was

verified through several experiments on silica substrates. After the 3-point alignment and the second layer of writefields were placed with corrected origo the same finalizing procedure as mentioned earlier was concluded.

4.2 Characterization of Particles

Characterization of nanoparticles can be done in multiple ways, depending on what information one is after. In this thesis the main focus is the particle shape, size and optical properties. Therefore, the Scanning Electron Microscopy (SEM) is a great option for investigating the physical dimensions, providing the user with clear images of particle size and shape. If hight of the particles was of any concern an Atomic Force Microscope (AFM) could be utilised. Optical properties are usually analysed through measuring of the absorption, scattering or emission of light from the sample, as this light will contain information about the sample [51]. The absorption and extinction spectra are of particularly interest when looking into a solar absorber. Therefore, an integrating sphere setup was chosen for optical characterisation.

4.2.1 SEM

The scanning electron microscope (SEM) was used to analyse the samples after the lift-off process and before the optical analyses. With the help of SEM images size, shape and particle placement could be measured. Lower magnification overview pictures were used to assess particle arrangement, write-field stitching and the amount of missing particles. Charge would accumulate on the surface of the non-conductive glass substrate, leading to distortion of the images. Higher voltages can lead to an image drift due to sample charging, therefore, a voltage of 1.75 kV and a aperture of 10 μm was used with the second electron (SE2) detector to achieve the best possible images. Håvardstun [38] demonstrated that the sample charging would lead to a shrinking effect of the measured particle sizes. This means that the imaged particles are seen to be smaller than what they really are. A solution to this would be to coat the sample with a conductive material and then measure the particle size. However as the optical characterisation was important, the larger arrays could not be coated to avoid this effect. On the other hand the dose matrices were coated with a 4 nm thick layer of gold-palladium as the structural dimensions were the only concern for those arrays. The gold-palladium layer was sputtered on with the sputter coater. Hence, the dose matrices could be evaluated with 10 kV voltage and 30 μm aperture using the InLens detector.

4.2.2 Integrated Sphere

To investigate the optical properties (transmission, reflectance and absorption) of the MNPs integrated spheres were chosen, which is depicted in Figure 4.5 and a schematic is shown in Figure 3.6. This setup can separate the contribution of absorption and scattering to the total extinction as it can directly measure the reflectance and transmittance (i.e. the scattering contributions) of the sample. In cooperation with the integrated spheres the computer software SpectraSuite was used as the data analyser. The y-axis on the plotted spectra (see Figure 5.20a) corresponds to the percentage of extinction (absorption) achieved. In other words, it is normalised to one. This is because the setup measures the percentage of reflected/transmitted light with regards to the reference spectra for reflectance/transmittance measurements. To check the reproducibility of the measurements each sample was measured three times, each time at different days.

This made it possible to check that results were in fact constant and not time dependent. Before the measurements could start the setup had to be calibrated. This was done by letting SpectraSuite set a integration time based on a reference spectrum. For transmission spectroscopy an empty transmission sphere was used as the reference, while for the reflection sphere a diffuse reference standard (WS-1 Reflectance standard) formed the spectrum. Integration time is the amount of time the spectrometer collects lights. Therefore, a longer integration time would result in a higher measured signal. However, too long integration time would lead to a saturation of the signal. Therefore, during calibration of the spectrometer the SpectraSuite software would set the integration time providing maximum signal without saturating the detector. Naturally transmittance and reflectance measurements would have different reference spectra. Therefore, a new calibration had to be done when changing from transmittance to reflectance or the other way around. These calibration had to be performed before every new measurement as dust could get into the system during sample placement, changing from reflectance to transmittance measurements etc. To improve the signal to noise ratio the software was set to average a certain number of scans. Another option to improve the signal to noise ratio was to increase the boxcar width, which is the amount of neighbouring points the scan will average over.

The integration times, scans to average and boxcar width are presented in Table 4.1. During the data analyses the measured intensities were normalised by dividing them on their respective integrations time.

TABLE 4.1: Calibration parameters for the integrated sphere setup.

Sphere	Integration time [ms]	Scans to average	Boxcar width
Reflection Sphere	383	20	2
Transmission Sphere	272	20	2

Several spectra was needed to calculate the extinction and absorption spectra of the MNP arrays. In this thesis the following measurements were obtained

- Transmittance spectrum of the sample ($I_{ST}(\lambda)$) and glass ($I_{GT}(\lambda)$), and the corresponding dark spectrum ($I_{STDark}(\lambda)$ and $I_{GTDark}(\lambda)$).

- Transmittance spectrum of an empty sphere (I_{StdT}), and the corresponding dark spectrum ($I_{StdTDark}$).

- Reflectance spectrum of the sample ($I_{SR}(\lambda)$) and glass ($I_R(\lambda)$), and the corresponding dark spectrum ($I_{SRDark}(\lambda)$ and $I_{GRDark}(\lambda)$).

- Reflectance spectrum of an empty sphere ($I_{SphereR}(\lambda)$) and the corresponding dark spectrum ($I_{SphereRDark}(\lambda)$).

- Reflectance spectrum of the reference standard ($I_{StdR}(\lambda)$) and the corresponding dark spectrum ($I_{StdRDark}(\lambda)$).

- Reflectance spectrum of the sample with the specular contribution removed.

- Dark reflectance spectrum of the glass with the specular contribution removed.

Each measurement was done by placing the sample in between the two spheres depicted in Figure 4.5, with the particles facing the light source. The reflection spectra

was measured through a sampling port in the reflection sphere, while the transmission spectra was gathered in the transmission sphere.

Transmittance and reflectance for the sample/glass substrates were then calculated by equation (2.40) and equation (2.39) respectively. It should be noted that when calculating the reflectance for the samples and glass substrate the reflectance contributions from the spheres itself is excluded. This was done to exclude the contribution from transmitted light reflected back into the reflecting sphere.
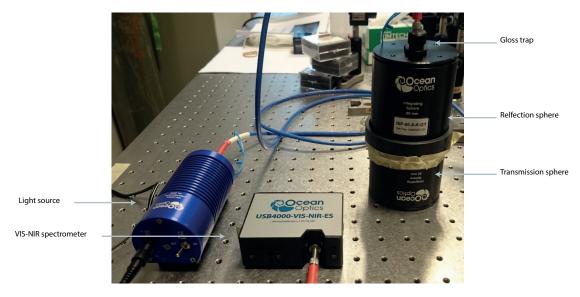

FIGURE 4.5: The integrated setup used in this work. The integrating spheres can be seen on the right.

Chapter 5

Experimental Results and Discussion

In the present section experimental investigation of the metal nanoparticle arrays will be discussed. The focus will be on particle shape, size as these are the deciding factors for LSPR. In addition to surface coverage (SC) which influences the maximum extinction achieved. The physical analysis is done by the means of SEM imaging, while a integrated sphere setup is used for the optical characterisation. The SEM characterisations will be discussed first as they lay the foundation for the interpretation of the optical results. The chapter will end with an in-depth discussion of the optical results based on the MNP properties, where extinction and absorption will be of main interest.

5.1 Samples

In total 13 large MNP arrays were produced by the means of EBL (see Chapter 4) for optical studies with an integrated sphere setup. The array size (9 mm^2) was chosen to exceed the size of the light spot (approximately 3 mm in diameter) used in the optical analyses. The arrays fall into two categories. The first category contain the arrays which consists of only one particle size throughout the entire array. The sample names, nominal diameter, interparticle distance (distance from centre to centre of two neighbouring particles) and height of these arrays are presented in Table 5.1. The second category contains the arrays with different sized particles and varying interparticle distance, these arrays are presented in Table 5.2. Two different resist schemes were used during the work in this thesis, single-layer scheme and a bi-layer scheme, see Section 3.3.1. However all of the presented work is produced on a bi-layer scheme. The establishment of an experimental procedure for creating large arrays consisting of different materials and MNPs was one of the objectives of this thesis work. This was achieved through the use of overlapping structures and alignment marks, the details are explained in Section 4.1.10.

The EBL writing parameters for the samples in Table 5.1 and Table 5.2 are presented in Table 5.3 and Table 5.4, the order in which the samples are presented does not indicate the order they were made. It should be noted that the reason why Au_120 has another interparticle distance in Table 5.3 than in Table 5.1 is due to an error in the CAD structure, which was not discovered until later when there was no time left for remaking the sample.

The original plan was to produce every particle size with the same voltage and aperture to avoid complications during the production of the multi particle arrays. Unfortunately an issue occurred while trying to manufacture the smallest particles (30 nm, 40 nm and 51 nm) with 20 kV voltage and 30 μm aperture in 3×3 mm^2 arrays. The problem was that the working distance was inconsistent due to a tilt in the sample, this resulted in a larger spot size as illustrated in Figure 5.1 which would lead to a reduction

in electrons per area. This was a problem for the smallest particles (< 55 nm) as their doses were already close to the clearance dose. To overcome this problem it was decided to decrease the aperture (explained in Section 4.1.5) which would lead to a better resolution. The idea behind this switch was that a higher resolution would mean that the doses needed for the small particles would be further away from the clearance dose limit, reducing the effect the tilt would have on the particles. The change in aperture would influence the final electron current reaching the sample surface, therefore new dose matrices had to be made.
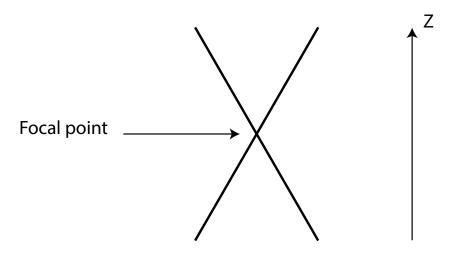
FIGURE 5.1: The intersecting lines represents how the focus of the SEM varies with Z (working distance). Ideal focus or rather ideal spot size is achieved at the intersection of the two lines, when Z is changed from this height the spot size will increase. This will lead to larger particles until the dose becomes lower than the clearance dose. The dose is in theory constant, however with a larger spot size the dose will be spread out on a larger area. Thus the dose per area will decrease with increasing spot size.

From the illustration in Fig 5.1 one can see that it does not matter if the sample is placed below or above the optimum working distance as the same increase in spot size would be experienced. Due to the tilt in the sample plane optimum focus could not be achieved for the entire array. Therefore, an average working distance based on the working distance just outside origo of the array and in the corresponding diagonal corner was set to compensate for the tilt.

As a result of the change in aperture for the smallest particles Au_mixed_array and Al_mixed_array had to be made as a two step procedure. Step one was to write the particles where an aperture of 20 µm was needed. Then for step two the aperture was changed to 30 µm and the rest of the array was written. The EBL writing parameters for Au_mixed_array and Al_mixed_array are presented in Figure 5.4. Au_Al_mixed_array were written with the same parameters as the arrays is a combination of Au_mixed_array and Al_mixed_array. The particles with diameters > 100 nm were created as ellipses with the long axis along the y-axis. This was done to correct for elliptical shape with the long axis along the x-axis experienced when creating circles in the CAD structure.

The height of the particles was intended to be 20 nm, however due to deposition of metal during the shutdown procedure (typically 2-3 nm) the final thickness is expected to exceed the nominal thickness (20 nm). Flatabø [29] found that the nominal thickness

was exceeded with approximately 5-6 nm for 20 nm films. However the film was highly uniform across the whole sample so that all nanoparticles can be taken to have the same height. This is a major advantage of the high quality electron beam evaporator in the UiB nanostructure laboratory.

TABLE 5.1: Sample name, nominal particle size and nominal interparticle distance for arrays with one particle size produced in this work. The samples are named according to the metal and nominal diameter respectively.

Sample name	Nominal diameter [nm]	Int.particle dist. (x,y) [nm]	Height [nm]
Au_200	200	600,600	20
Au_150	150	450,450	20
Au_120	120	360,360	20
Au_100	100	300,300	20
Au_80	80	240,240	20
Au_60	60	180,180	20
Au_45	45	150,150	20
Al_200	200	600,600	20
Al_150	150	450,450	20
Al_120	120	360,360	20

TABLE 5.2: Sample name, nominal particle size and nominal interparticle distance for arrays with more than one particle size produced in this work. The samples are named according to the metal and nominal diameter respectively.

Sample name	Nominal diameter [nm]	Int.particle dista. (x,y) [nm]	Height [nm]
Au_mixed_array	30	173,173	20
	51	173,173	20
	76	173,173	20
	110	330,173	20
Al_mixed_array	40	173,173	20
	61	173,173	20
	79	173,173	20
	104	330,173	20
	115	345,173	20
Au_Al_mixed_array	40	173,173	20
	30	173,173	20
	61	173,173	20
	51	173,173	20
	79	173,173	20
	76	173,173	20
	104	330,173	20
	110	330,173	20
	115	345,173	20

TABLE 5.3: EBL writing parameters for the single particle arrays.

	Au_200	Au_150	Au_120	Au_100	Au_80	Au_60	Au_45	Al_200	Al_150	Au_120
Resist scheme	bi-layer	bi-layer	bi-layer	bi-layer	bi-layer	bi-layer	bi-layer	bi-layer	bi-layer	bi-layer
Nominal NP diameter [nm]	200	150	120	100	80	60	45	200	150	120
CAD NP diameter (x,y) [nm]	160,168	120,126	96,101	80,84	dot	dot	dot	160,168	120,126	96,101
Int.particle distance (x,y) [nm]	600,600	450,450	420,420	300,300	240,240	180,180	150,150	600,600	450,450	360,360
Array area [mm^2]	3×3	3×3	3×3	3×3	3×3	3×3	3×3	3×3	3×3	3×3
Theoretical SC (%)	8.72	8.72	6.41	8.72	8.72	8.72	7.07	8.72	8.72	8.72
Number of particles ($\cdot 10^6$)	26.7	47.4	54.5	106.7	166.7	296.3	426.7	26.7	47.4	74.1
Acceleration voltage (kV)	20	20	20	20	20	20	20	20	20	20
Aperture [µm]	30	30	30	30	30	30	20	30	30	30
Measured beam current [nA]	0.309	0.309	0.309	0.309	0.306	0.306	0.142	0.308	0.306	0.306
Nominal exposure dose [µC/cm^2]	120	120	120	120	0.0045*	0.0045*	0.006*	120	120	120
Dose factor	1.585	1.4	1.3	1.3	1.65	1.3	1.1	1.585	1.4	1.31

* = dot exposure has units [pC]

TABLE 5.4: EBL writing parameters for the multi particle layers. Au_Al_mixed_array was written with the same parameters presented in this table.

	Au_mixed_array				Al_mixed_array				
Resist scheme	bi-layer	bi-layer	bi-layer	bi-layer	bi-layer	bi-layer	bi-layer	bi-layer	bi-layer
Nominal NP diameter [nm]	30	51	76	110	40	61	79	104	115
CAD NP diameter (x,y) [nm]	dot	dot	dot	88,92	dot	dot	dot	84,88	92,96
Int.particle distance (x,y) [nm]	173,173	173,173	173,173	330,173	173,173	173,173	173,173	330,173	345,173
Array area [mm^2]	3×3	3×3	3×3	3×3	3×3	3×3	3×3	3×3	3×3
Number of particles ($\cdot 10^6$)	99.9	8.6	8.6	8.6	91.6	8.6	8.6	8.6	8.6
Theoretical SC (%)	0.9	0.2	0.4	0.9	1.5	0.3	0.4	0.8	0.9
Acceleration voltage (kV)	20	20	20	20	20	20	20	20	20
Aperture [μm]	20	20	30	30	20	30	30	30	30
Measured beam current [nA]	0.142	0.142	0.305	0.305	0.142	0.305	0.305	0.305	0.305
Nominal exposure dose [μm/cm^2]	0.006*	0.006*	120	120	0.006*	120	120	120	120
Dose factor	0.42	1.45	1.45	1.3	0.7	1.15	1.5	1.3	1.3
Writing time [hour]	20.5				17.3				

* = dot exposure has units [pC]

5.2 Structural Analyses

The analyses of size, shape, interparticle distance and surface coverage (SC) of the nanoparticle arrays is the main objectives for the structural analyses in this work, in addition the amount of missing particles and particle displacement were also investigated. The former is important for the overall optical performance of the array. The latter is not so critical provided the displacement is so small that it will not lead to an optical coupling between the particles. These properties are investigated by means of the SEM.

The fact that the nanoparticles are placed on an insulating glass substrate causes a special experimental challenge. This was caused by the gradual charging of the substrate during imaging, which leads to image distortion and a drift. Therefore, a low acceleration voltage of 1.75 kV and a small 10 μm beam aperture was chosen. The problem could be eliminated by coating the wafer with a conductive layer (e.g. chromium). However the conductive layer would interfere with the optical measurements and thus, was not a viable option. Although the low acceleration voltage reduced the charging effects, the drift caused by it was still present in the system, causing a distortion in the images taken at a low scan speed.

A tilt varying with every wafer was present during the writing process of the arrays. This resulted in a sub optimum focus throughout the writing procedure as discussed in the previous section. Therefore, the average working distance between two points on the sample was set as the working distance. Thus the optimum focus should in theory be in the centre of the sample, and deteriorate in all directions when leaving the centre. This leads to larger particles as you leave the centre, however this effect was not explicitly experienced. The tilt is a known issue when producing arrays of this size, as usually EBL is used to produce particles in smaller arrays. The exact behaviour due to the tilt is still not completely understood. An attempt to neutralize the tilt was made by substituting the Borosilicate glass substrates with a thicker and flatter substrate, the idea being that the tilt is due to the clips holding the sample in the sample holder. Unfortunately no particles were found on the substrate during imaging after developing and lift-off had been completed. It was believed that this came from a low adhesion between the MNPs and the substrate.
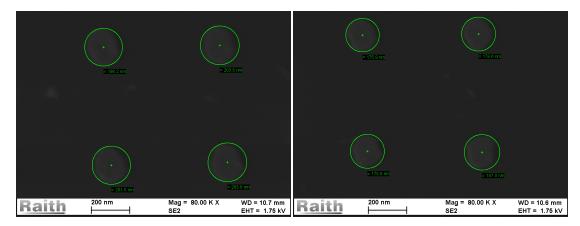
For the experiments presented here, four particles and two interparticle distances were measured five times in the four corners and in the centre of the array. This selection was assumed to be representative for the entire array. Table 5.5 presents the average particle diameter, interparticle distance in x and y direction for the single particle arrays. The surface coverage for the single particle arrays is presented in Table 5.6. The measured structural dimensions for the mixed particle arrays are presented in Table 5.7. The errors are presented as standard deviations. Strictly speaking standard deviation is not the best suited statistics to quantify the systematic error caused by the tilt, but it does makes it possible to compare results in a quick manner.

The e_Line software has a built-in working distance correction tool, which in theory should be able to calculate the tilt of the surface plane based on the working distance measured at three different locations. The software would then adjust the working distance accordingly. This was seen as a solution to the problems caused by the tilt, and it was implemented in the production of the dose matrices. As promising results were seen, the procedure was deemed viable and implemented in the production of all the large arrays. In an effort to be time and cost effective all of the arrays were fabricated with the e_Line before development and lift-off were attempted. During lift-off it became clear that the writing procedure had failed and that there were practically no particles on the substrates, this was confirmed by SEM images. This failure was attributed to the fact

that the software did not manage to calculate the tilt correctly, leading to the wrong working distance being set by the software. Accordingly the clearance dose was not reached and no clear patterns were created in the PMMA. This set back made it clear that the tilt correction was not a viable option when reproducing the arrays, hence the previously mentioned averaging technique was implemented instead. Further research into the tilt correction tool is planned within the group.

In addition to the drift caused by the charging effect, a drift within the system was experienced, causing a displacement of the second row of particles imaged. This also increased the distortion of the images and variation in interparticle distances, especially in the y-direction. The drift within the system can be attributed to the temperature fluctuations experienced in the ISO 7 clean room. The temperature within the e_Line cabinet was set to 18.5°C. This however would fluctuate due to a shifting temperature in the surrounding room related to a problem with the overall cooling system that occurred during the experiments. This was especially a problem if the temperature in the room where the e_Line cabinet is located was set too low, then the air condition would not work properly and fluctuations up to 1°C could be experienced. The latter temperature fluctuation was fixed at a later stage of the experimental work. Another problem during the writing procedure was the ongoing construction and maintenance work being done outside of the UiB nanostructure laboratory, leading to unwanted vibrations in the building. This external vibration could lead to distortions and slightly misplaced particles. The effect of these vibrations were visible (astigmation and drift) during the SEM imaging of a couple of the arrays. The characterisation was therefore postponed until the construction workers had left for the day. However, a few of the arrays had to be written during the day and it is clear that the vibrations would influence the final result. The exact MNP location is not important as long as the interparticle distance and the intended structure is as intended.

5.2.1   Analysis of Single Particle Diameter Arrays
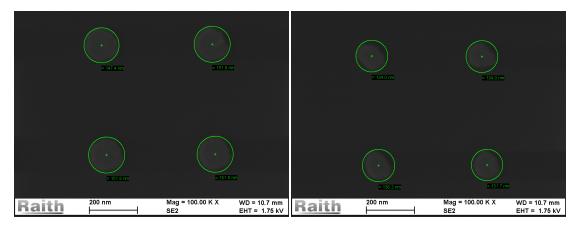
SEM images of Au_200 are presented in Figure 5.2, the majority of the particles are in the same size range. When comparing Figure 5.2a with Figure 5.2b it is seen that even though the standard deviation for the arrays is low (197 nm ± 7 nm) some particles deviates significantly from the rest. However, as the standard deviation is low this disparity will not drastically affect the optical analysis. The observed particles are not perfectly circular, which could influence the optical properties of the MNPs. This disparity in shape could be caused by astigmation during the imaging process. As explained in Section 4.1.5 astigmation occurs when the focal length is longer in either the x- or y-direction. To avoid this, the stigmation is adjusted prior to the imaging. It is hard to achieve a perfect stigmation on a glass substrate when charging occurs, hence the elliptical shape could be due to a sub optimum stigmation and not a physical property of the particles. To verify this the arrays have to be coated with a conductive layer and imaged a second time. The other explanation is that a drift was present during the writing, which resulted in a slightly prolonged y-axis.

(A) SEM image of Au_200 used to determine (B) SEM image of Au_200 particles showing the
particle size and interparticle distance. particle size variation within the array.
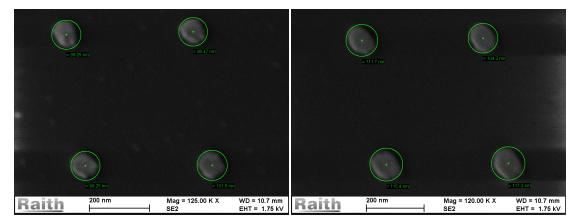
FIGURE 5.2: SEM images of Au_200 used to determine particle size
and interparticle distance. The average particle diameter was found
to be 197 nm $\pm$ 7 nm, with interparticle distance 606 nm $\pm$ 6 nm and
617 nm $\pm$ 9 nm in the x-direction and y-direction respectively.

The SEM images of Au_150 in Figure 5.3a and Figure 5.3b displays the same variation in particle size as seen for Au_200 in Figure 5.2. Therefore, it is probably the same problem influencing the writing procedure, where the most probable explanation is the tilt. Another fact to note is the deviation from a circular shape, especially for the particles furthest away from 150 nm. These particles exhibits an elliptical shape with long axiz along the y-axis.

(A) SEM image of Au_150 used to determine (B) SEM mage of Au_150 particles showing the
particle size and interparticle distance. particle size variation within the array.

FIGURE 5.3: SEM image of Au_150 used to determine particle size
and interparticle distance. The average particle diameter was found
to be 148 nm $\pm$ 5 nm, with interparticle distance 452 nm $\pm$ 8 nm and
449 nm $\pm$ 8 nm in the x-direction and y-direction respectively.

(A) SEM image of Au_120 used to determine particle size and interparticle distance.

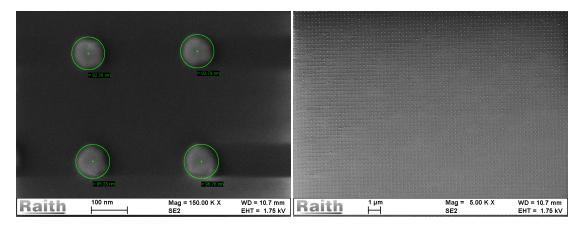(B) SEM image of Au_120 particles showing the particle size variation within the array.

FIGURE 5.4: SEM image of Au_120 used to determine particle size and interparticle distance. The average particle diameter was found to be 102 nm $\pm$ 7 nm, with interparticle distance 423 nm $\pm$ 3 nm and 432 nm $\pm$ 7 nm in the x-direction and y-direction respectively.
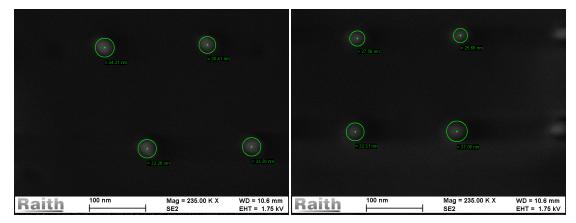
The particles in Au_120 which are seen in Figure 5.4 have a particle diameter of 102 nm $\pm$ 7 nm, which is 16 % lower than the expected particle size of 120 nm. The reason for this discrepancy is not known, but the most plausible explanation is the shrinking effect explained in Section 4.2.1. That is, due to accumulation of charge on the substrate, the particles seems to shrink, and a too low diameter is measured. Au_120 and Al_120 were made with the same EBL writing parameters (except for the change in interparticle distance) and thus the two arrays should be comparable. However, a discrepancy in particle size is seen. The particle diameter in Al_120 (which is seen in Figure 5.10a) was found to be 10 % larger than that of Au_120, a rather unexpected difference. Both of the arrays were produced with a minimum interparticle distance of three times the diameter, which is why the proximity effect should not influence either of the arrays. Hence the most plausible explanation for this discrepancy is the previously mentioned tilt. Furthermore when comparing Figure 5.4a and Figure 5.4b the effect of the drift during imaging is seen, as the second row of particles is shifted further to the right.

(A) SEM image of Au_100 used to determine particle size and interparticle distance.

(B) SEM image of Au_100 particles showing the particle distribution within the array.

FIGURE 5.5: SEM image of Au_100 used to determine particle size and interparticle distance. The average particle diameter was found to be 96 nm ± 4 nm, with interparticle distance 302 nm ± 5 nm and 303 nm ± 8 nm in the x-direction and y-direction respectively.

Figure 5.5b shows an overview image of the Au_100 from the centre of the array, a few particles are missing and some have drifted to another position in the array. These holes and position shifts are due to the lift-off process and a low adhesion between glass and gold nanoparticles. The rearrangements are not seen as vital enough to influence the optical results. The particles within Au_100 were found to be circular, and only a 4 % difference between the nominal diameter and measured diameter was found.

(A) SEM image of Au_60 used to determine particle size and interparticle distance.
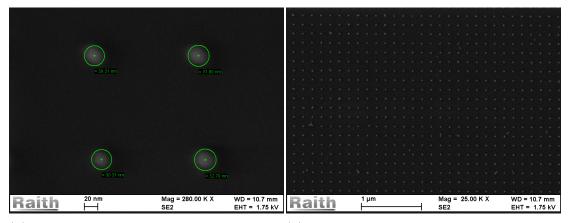
(B) SEM image of Au_60 particles showing the particle size variation within the array.

FIGURE 5.6: SEM image of Au_60 used to determine particle size and interparticle distance. The average particle diameter was found to be 36 nm ± 5 nm, with interparticle distance 182 nm ± 4 nm and 181 nm ± 12 nm in the x-direction and y-direction respectively.

As seen when comparing Figure 5.6a and Figure 5.6b the drift experienced during SEM imaging was varying throughout the imaging process, resulting in an increase in interparticle distance (especially in the y-direction). This explains the jump in standard deviation compared to the other obtained values. Furthermore it also confirms that it was not a systematic drift, as it would change throughout the array. This drift was

attributed to temperature fluctuations in the clean room cabinet where the e_Line is placed and possible vibrations in the building as discussed above. The difference in nominal particle diameter and measured particle diameter for Au_60 is 50 %, which is higher than what the previously mentioned shrinking effect has been found to cause in previous work. Due to this it is unlikely that the charging effect alone is behind the disparity, the other probable contributor is a low exposure dose. However to verify this the arrays have to be coated with a conductive layer and analysed again with the SEM. This was not done as the conductive layer would interfere with the optical analyses.

SEM images of Au_45 is shown in Figure 5.7, and the measured particle diameter is 34 nm $\pm$ 3 nm. This is a difference of 27 % from the nominal diameter. The plausible explanation for this is the experienced shrinking caused by the charging effect.
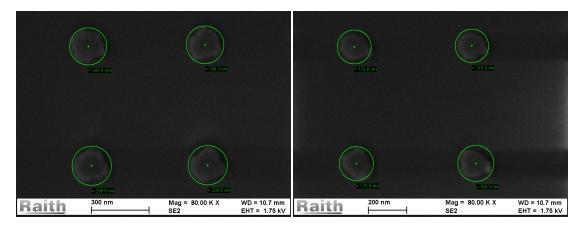
(A) SEM mage of Au_45 used to determine particle size and interparticle distance.

(B) SEM image of Au_45 particles showing the particle distribution.

FIGURE 5.7: SEM image of Au_45 used to determine particle size and interparticle distance. The average particle diameter was found to be 34 nm $\pm$ 3 nm, with interparticle distance 152 nm $\pm$ 2 nm and 157 nm $\pm$ 3 nm in the x-direction and y-direction respectively.

Figure 5.7b shows no holes in the array. However some particles seems to have drifted in from other positions within the array, hence there should be some holes in the neighbouring area. The defects in the array are so few that they should not influence the optical properties investigated in the integrating spheres.
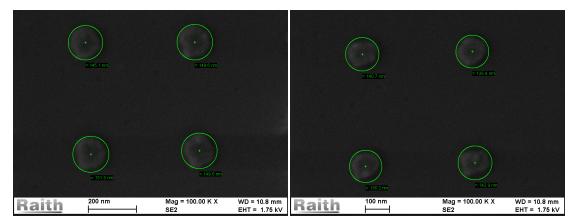
The Al_200 particles in Figure 5.10 were found to have a circular shape, although with a lower diameter than intended. When compared to the Au_200 array in Figure 5.2 the particles are found to be smaller. The interparticle distances are equal, therefore proximity effect is unlikely to be the cause of this discrepancy. As mentioned earlier the tilt could lead to larger particles, which is the probable explanation to the difference in diameter. To avoid these problems the tilt has to be reduced to a minimum or eliminated. Figure 5.8a and Figure 5.8b shows particles from two corners in the array diagonally across each other. The discrepancy in particle size is attributed to the tilt.

(A) SEM image of Al_200 used to determine particle size and interparticle distance.

(B) SEM image of Al_200 particles showing the variation in particle size.

FIGURE 5.8: SEM image of Al_200 used to determine particle size and interparticle distance. The average particle diameter was found to be 192 nm $\pm$ 7 nm, with interparticle distance 606 nm $\pm$ 5 nm and 612 nm $\pm$ 8 nm in the x-direction and y-direction respectively.

In Figure 5.9b SEM images of Al_150 is presented. The measured particle size for this array was 146 nm $\pm$ 5 nm, compared to the measured particle diameter of 148 nm $\pm$ 5 nm for Au_150. Thus, the two arrays are structurally similar.
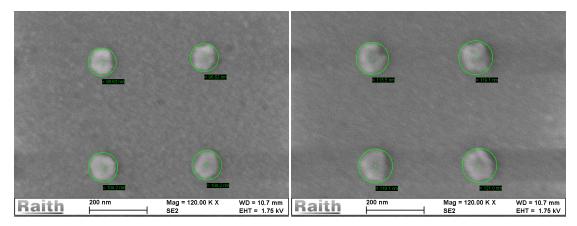
(A) SEM image of Al_150 used to determine particle size and interparticle distance.

(B) SEM image of Al_150 particles showing the variation in particle size.

FIGURE 5.9: SEM image of Al_150 used to determine particle size and interparticle distance. The average particle diameter was found to be 146 nm $\pm$ 5 nm, with interparticle distance 453 nm $\pm$ 4 nm and 459 nm $\pm$ 5 nm in the x-direction and y-direction respectively.

Figure 5.9a shows the particles in a corner of the array, while Figure 5.9b was taken in the middle of the array. The discrepancy in size is expected due to the tilt and the varying working distance. As previously explained larger particles are expected away from the centre of the array.

Figure 5.10 presents SEM images of the Al_120 array. The particles were found to have a diameter of 113 nm $\pm$ 5 nm, slightly bigger than the particles in Au_120. As mentioned above this variation in size is caused by the tilt. Figure 5.10b shows that the

particle sizes in the array could vary within small areas. However, it was found that this did not influence the optical analyses.

(A) SEM image of Al_120 used to determine particle size and interparticle distance.

(B) SEM image of Al_120 particles showing the variation in particle size.

FIGURE 5.10: SEM image of Al_120 used to determine particle size and interparticle distance. The average particle diameter was found to be 113 nm ± 5 nm, with interparticle distance 361 nm ± 2 nm and 372 nm ± 3 nm in the x-direction and y-direction respectively.

The obtained structural dimensions for the arrays are presented in Table 5.5.

TABLE 5.5: Obtained structural dimensions for the single particle arrays. Au_80 was not measured due to downtime in the UiB nanostructure laboratory.

Sample Name	NP diameter [nm]	Int.particle dist. (x) [nm]	Int.particle dist. (y) [nm]
Au_200	197 ± 7	606 ± 6	617 ± 9
Au_150	148 ± 5	452 ± 8	449 ± 8
Au_120	102 ± 7	423 ± 3	432 ± 7
Au_100	96 ± 4	302 ± 5	303 ± 8
Au_80			
Au_60	36 ± 5	182 ± 4	181 ± 12
Au_45	34 ± 3	152 ± 2	157 ± 3
Al_200	192 ± 7	606 ± 5	612 ± 8
Al_150	146 ± 5	453 ± 4	459 ± 5
Al_120	113 ± 5	361 ± 3	372 ± 5

The surface coverage for every array was calculated based on the obtained structural dimensions presented in Table 5.5. The values are presented in Table 5.6 and can be compared to the theoretical surface coverage values found in Table 5.3. The theoretical values are found to be higher than the calculated values, especially for the smaller particle arrays. This disparity is attributed to the difference in measured structural dimensions and theoretical dimensions. The decrease in surface coverage will reduce the maximum extinction measured in the optical analyses.

TABLE 5.6: Calculated surface coverage for the single particle arrays. The calculations are based on the obtained structural dimensions presented in Table 5.5. Surface coverage was not calculated for Au_80 as SEM images of the arrays were not obtained.
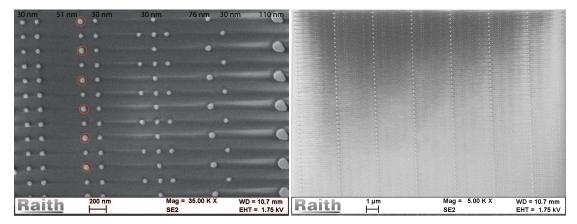
Sample name	Surface coverage [%]
Au_200	8.2 ± 0.1
Au_150	8.5 ± 0.2
Au_120	4.5 ± 0.1
Au_100	8.0 ± 0.3
Au_80	
Au_60	3.3 ± 0.2
Au_45	3.8 ± 0.1
Al_200	7.8 ± 0.1
Al_150	8.1 ± 0.1
Al_120	7.5 ± 0.1

Unfortunately it was not possible to obtain SEM images of Au_80 due to unexpected downtime in the UiB nanostructure laboratory. The array was still included for optical analyses.

5.2.2 Analysis of Mixed Arrays

Due to the troubles with recreating sub 55 nm particles in the big arrays, it was decided to create the smallest particles with a lower aperture. Unfortunately time limitations prevented correct doses to be found for the larger particles on the new aperture setting. This resulted in the three mixed arrays being produced with two different aperture settings. The measured particle diameters, interparticle distances and calculated surface coverage for Au_mixed_array and Al_mixed_array are presented in Figure 5.7.
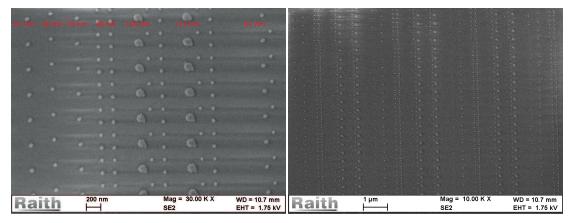
(A) SEM image of Au_mixed_array and the particle structure within the array.

(B) Overview image of the array. The observed shadow effect is due to sample charging.

FIGURE 5.11: SEM images of the Au_mixed_array. The red circles indicates which particles that have a diameter of 51 nm. The measured particle sizes are presented in Table 5.7.

The SEM image in Figure 5.11a presents the mixed array structure. It shows a displacement of the 76 nm and 110 nm gold particles compared to that of the CAD structure in Figure 4.4b. The 76 nm particles should have been in the left opening of the third 30 nm particle row, while the 110 nm particles should have been where the 76 nm particles are now. When writing Au_mixed_array and Al_mixed_array the 40 nm, 30 nm and 51 nm particles were written first with an aperture set to 20 μm and a acceleration voltage set to 20 kV. The 61 nm, 79 nm, 76 nm, 104 nm, 110 nm and 115 nm particles used a 30 μm aperture and a 20 kV acceleration voltage. Ideally these particles would have been created in the same CAD structure although in different layers, two layers containing the gold NPs and two layers containing the aluminium NPs. However, a very long estimated writing time for each of the layers were calculated. Initially this was believed to be caused by the many layers implemented. Therefore, as a quick solution to this each of the layers were recreated in their own CAD structure. The problem with this, which was noticed during SEM imaging of the mixed arrays, was that even though particles were placed in the exact same position as in the previously used layers, the software would interpreted the first placed particle to be in the origo of the writefield. Therefore, when the second layer was placed in the position list with the same origo as the first layer, a shift in particle placement occurred. The shift is seen in Figure 5.11a. This error would propagate through the array and therefore the shift is different depending on where in the array images were taken.

The same misalignment of the two CAD structures as seen in Figure 5.11 can be seen in Figure 5.12 for the Al_mixed_array. However, for Al_mixed_array the relative shift between the two CAD layers were constantly changing trough the array. It was therefore decided to measure the interparticle distance between particles in their respective layers. The 40 nm particles were written in the first layer, while the 61 nm, 79 nm, 104 nm and the 115 nm particles were written in the second layer. The shift in particle placement is mainly in the x-direction, while only a small displacement in experienced in the y-direction.

(A) SEM image of Al_mixed_array and the particle structure within the array.

(B) Overview image of the array. The observed shadow effect is due to charging.

FIGURE 5.12: SEM images of the Al_mixed_array. The measured particle sizes are presented in Table 5.7.

TABLE 5.7: Obtained structural dimensions for Au_mixed_array and Al_mixed_array.

	Au_mixed_array				Al_mixed_array				
Nominal NP diameter [nm]	30	51	76	110	40	61	79	104	110
Measured NP diameter [nm]	64 ± 8	81 ± 8	81 ± 11	163 ± 10	47 ± 7	69 ± 9	67 ± 11	133 ± 12	144 ± 11
Int.particle distance (x) [nm]	170 ± 5	180 ± 4	277 ± 147	182 ± 14	181 ± 8	682 ± 10	844 ± 17	678 ± 10	1026 ± 22
Int.particle distance (y) [nm]	173 ± 8	169 ± 7	348 ± 17	342 ± 4	172 ± 10	350 ± 12	351 ± 11	350 ± 14	351 ± 11
Surface coverage [%]	4.2 ± 0.2	0.48 ± 0.05	0.32 ± 0.04	1.0 ± 0.5	2.3 ± 0.2	0.17 ± 0.02	0.21 ± 0.04	0.62 ± 0.02	0.7 ± 0.1

The high discrepancy in nominal particle diameter and measured diameter was found to be related to a problem within the CAD structure. At a late stage in this work it was discovered that in the CAD structure for the mixed_arrays particles were duplicated inside the structure. In other words, one position would contain several overlying particles resulting in a higher dose than intended. There was no evidence of this being an systematic error as the amount of overlying particles varied throughout the entire structure. This also explains why the standard deviations are as high as they are compared to that of the single particle arrays.

As explained above Au_200, Au_150 and Au_100 have measured particle sizes and surface coverage close to the expected values. Indicating that in fact the measured extinction and absorption spectra for those arrays would be representative for the intended individual particles. Au_120 on the other hand was produced with the wrong interparticle distance and the particles were measured to be 102 nm ± 7 instead of 120 nm. This resulted in the surface coverage being reduced by 63 %, which will influence the extinction maxima found in the optical analyses. Hence the optical results will represent that of a poorly covered 100 nm array. This is why the array is comparable to Au_100 with regards to the full-widt-half-maximum (FWHM) of the extinction spectrum and the peak position.

Au_60 an Au_45 were found to have particles in the 36 nm and 34 nm range respectively, again reducing the surface coverage of the array. This would influence the extinction peak maxima, however peak position should be independent of the change in surface coverage.

Al_200 and Al_150 both had measured particle diameters and surface coverage close to the nominal values. Therefore, the optical analyses of those arrays will be representative for 200 nm and 150 nm aluminium particles. In addition the particles were statistical comparable to that of Au_200 and Au_150 respectively, providing a foundation for comparison between gold and aluminium particles of the same size.

Al_120 on the other hand was found to contain smaller particles than intended, 113 nm ± 5 nm. Therefore, the optical analyses of this array has to be seen as representative for 113 nm particles instead of 120 nm particles. In addition it was found that Au_120 contained smaller particles than Al_120. This makes it difficult to properly compare the optical results for the two arrays.

The two mixed arrays that were imaged in the SEM were found to contain much larger particles than expected due to a duplication issue in the CAD structure. An increase in particle size will redshift the LSPR peak, hence it is important to keep in mind the actual diameter of the particle when comparing results. Furthermore, the shift between the two layers used in the writing process lead to particles having interparticle distances smaller than three times the diameter. It would thus be logical to expect near-field coupling in the regions were that happened. However, this should only be in small parts of the array and should not influence the optical properties excessively. Although a small redshift of the LSPR peak could be experienced, this would however be hard to quantify.

Unfortunately the Raith e_Line experienced some downtime, which meant that the Au_80 and Au_Al_mixed_array could not be investigated in the SEM. However Au_Al_mixed_array was made with Au_mixed_array as the foundation, providing some insight in the diameter of the gold particles and their distribution. In addition the aluminium pattern was created with the same CAD structures as Al_mixed_array, hence a general composition of the array can be estimated. Due to the lack of SEM images nothing exact can be said about particle placement and interparticle distance.

Therefore, near-field coupling could occur resulting in a shift of the LSPR peaks. In regards to Au_80, only a visual inspection was possible, and based on this it was assumed that particles in the array were smaller than the planned 80 nm. This conclusion was drawn as the array itself was almost invisible to the naked eye, while, for example the Au_60 arrays was possible to see.

In general the increase or decrease in particle diameter was not of major concern, as the goal of the thesis was to find the correct particle composition to create a solar absorber. Therefore, as long as the measured extinction and absorption spectra are connected to the actual particle sizes, a proposal can be made.

5.3   Optical analyses

When making a solar absorber based on MNPs, the extinction and absorption of the respective particles are important. Extinction and absorption are discussed in Section 2.4, however a short a explanation is given here. Absorption, when talking about absorption of electromagnetic radiation, is a measure of the fraction of incoming photons that is taken up by matter (in our case MNPs). Extinction is the sum of the fraction of light absorbed by the matter and light scattered by the matter (MNPs in the solar absorber). Here scattering is light redirected by the MNPs without other changes to optical properties occurring (e.g. frequency, polarization and wave number) [42]. For nanoparticles on a thin transparent substrate it can be assumed that no light scatters and that therefore extinction is equal to absorbance (see below). Using the integrated sphere setup transmittance and reflectance (background contribution, in principle the sample has no reflectance) is easily obtained. The absorption can then be found through energy conversion, as discussed in Section 2.4

$$1 = \text{Transmittance (T)} + \text{Reflectance (R)} + \text{Absorption (A)} . \qquad (5.1)$$

Extinction on the other hand is the attenuation of transmitted light through matter [43] and calculations of the extinction were done by the relation

$$\text{Extinction} = \text{Absorbance} = -\log(\text{Transmittance}) . \qquad (5.2)$$

This is valid for particles on a thin transparent substrate (no light is reflected) as discussed above [46]. Absorbance is the attenuation of transmitted radiant power, while absorption is the physical process of absorbing light [42]. The extinction peak of aluminium particles with D < 120 nm were expected to be outside the spectral range of the current light source and optical fibre. Thus it was decided to not produce aluminium arrays with D < 120 nm. Extinction and absorption is plotted as a function of the incident wavelength in the 400 nm - 900 nm range due to the limitations of the light source. Each sample was measured on three different days to investigate the reproducibility of the experiment. Even though the MNP arrays were made bigger than the light spot (3 mm) it proved difficult to place the samples in the exact same position every time during measurements, hence a variation in measured spectra were seen. Therefore, two samples were measured 5 additional times while taking extra care to get the array placed in the middle of the light source. The results are discussed in the end of this chapter and presented in Figure 5.26. The measured extinction/absorption peaks and positions are presented in Table 5.8. The errors were calculated as standard deviations based on the different measurements.

5.3.1 Analysis of Single Particle Diameter Arrays

In Figure 5.13 extinction and absorption spectra for Au_200 is presented. The particles have a diameter of 197 nm ± 7 nm and an interparticle distance of 606 nm ± 6 nm in the x-direction and 617 nm ± 9 nm in the-y direction. The broad extinction peak is attributed to the spread in particle diameter. A known feature for LSPR is its dependence of size where increasing diameters results in a redshift of the LSPR peak [52]. Hence when the array has a variation in the particle sizes the full-widt-half-maximum will broaden. Deviations in a particles circular shape would lead to a blueshift of the peak [53] and contribute to the broadened peak.
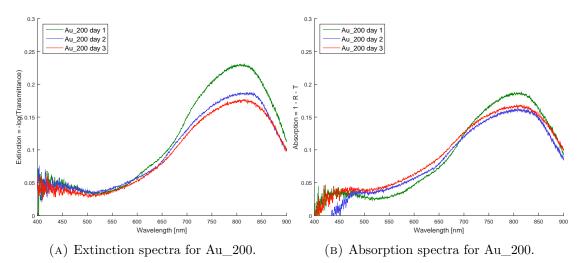
(A) Extinction spectra for Au_200.	(B) Absorption spectra for Au_200.

FIGURE 5.13: Measured extinction and absorption spectra for Au_200 carried out at three different days to investigate the measurement reproducibility. The broadened peaks is due to the variation in particle size within the sample. The similar extinction and absorption spectra tells us that absorption interactions dominates over scattering.

The absorption and extinction spectra are quite similar in both intensity and shape, as expected if the scattering can be neglected (see the discussion in the previous section). The variation in measured extinction and absorption from day to day is most likely due to the sample being placed at different spots during each measurement, this is discussed at the end of this section.

Au_150 consists of particles with a diameter of 148 nm ± 5 nm. The size and shape distribution within the array is relatively small leading to narrow extinction and absorption peaks. As expected the extinction/absorption peak is blueshifted with regards to Au_200 due to the decrease in particle size [41]. An increase in extinction and absorption maxima is experienced when compared to the Au_200 array. This is caused by the increased surface coverage and the smaller variation in particle size/shape within the Au_150 array. Variation in particle size results in a lower surface coverage of each particle diameter present in the array. Basically, you have fewer particles absorbing at a specific wavelength and the absorption is spread out over a larger range of wavelengths.
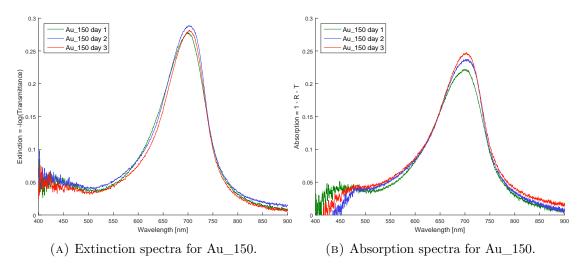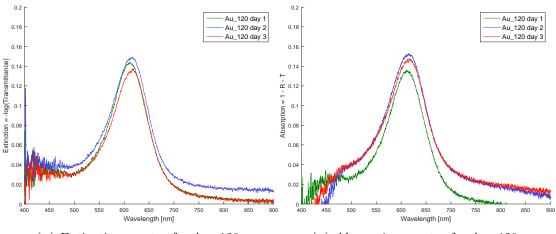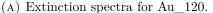
(A) Extinction spectra for Au_150. (B) Absorption spectra for Au_150.

FIGURE 5.14: Measured extinction and absorption spectra for Au_150.
The peaks are narrow, indicating an insignificant variation in particle
diameter and size within the array.

Interestingly enough day 2, has the highest extinction spectra, while day 3 has the highest absorption spectra. This could indicate that the placement of the sample would influence absorption and scattering properties within the arrays, due to a variation in the particle size distribution across the array.

As expected the maxima extinction and absorption peaks are lower for the Au_120 array than for Au_200, Au_150 and Au_100 because the surface coverage is smaller. The drop in surface coverage from Au_150 to Au_120 is 62 %, while the corresponding reduction in extinction is 64 %. This confirms the expected linear relationship between extinction and surface coverage. The difference of 2 % is due to the issues of placing the array in the integrated sphere in the perfect position. The particles within the array were found to have a diameter of 102 nm $\pm$ 7 nm, hence these results are not representative for gold particles with a diameter of 120 nm. Comparing them with the Au_100 array on the other hand is quite interesting as the particles in Au_100 have a diameter of 96 nm $\pm$ 4 nm. Statistically the particle diameter within these two arrays could be equal, however there is a difference of 56 % in surface coverage for the arrays. This explains why Au_100 has the highest extinction peak of the two. Peak position is also found to differ for the two arrays, Au_120 has its peak at 615 nm $\pm$ 3 nm where Au_100s peak is found at 587 nm $\pm$ 1 nm. The difference in particle size for the two arrays is 6 %, while the difference in peak position is 5 %, indicating a linear relationship between particle size and peak position. However this trend is not seen when other arrays are compared in a similar way. This indicates that the linear trend is only applicable when the particle-size difference is low.

(A) Extinction spectra for Au_120.   (B) Absorption spectra for Au_120.

FIGURE 5.15: Measured extinction and absorption spectra for Au_120.
The lowered intensity compared to Au_100 is attributed to the wrong
interparticle distance used resulting in a sub optimum surface coverage.

(A) Extinction spectra for Au_100.   (B) Absorption spectra for Au_100.
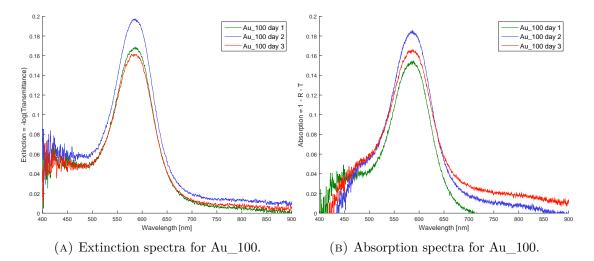
FIGURE 5.16: Measured extinction and absorption spectra for Au_100.
The narrow peaks indicates a negligible particle variation within the array.

Figure 5.17 shows the extinction and absorption spectra for Au_80, which turned
out to be an array with much smaller particles than planned. This decrease in particle
size had a drastic impact on the surface coverage for the array. hence the measured
extinction/absorption spectra are low. Another issue with this sample was that the
array on the substrate was nearly invisible to the naked eye. Therefore, it was difficult
to ensure that the array was actually placed within the light spot. This is quite clear
from Figure 5.17 as it resulted in a highly varying spectra. By comparing the extinction
peak position to Au_80 in Figure 5.17a to that of Au_60 in Figure 5.18a and Au_45 in
Figure 5.19a it is possible to estimate the particle size in the Au_80 array. The extinction
peak to Au_80 is slightly blueshifted compared to that of Au_60 and Au_45. In other
words the particles in Au_80 should be in the range of 30 nm - 34 nm.

(A) Extinction spectra for Au_80.

(B) Absorption spectra for Au_80.
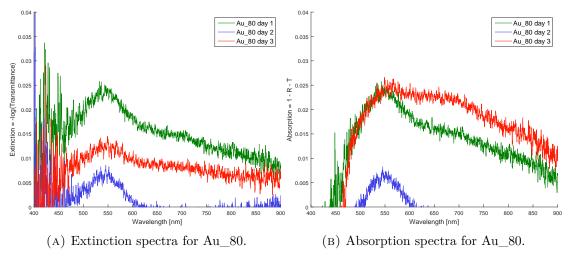
FIGURE 5.17: Measured extinction and absorption for Au_80. The low extinction value is due to the low surface coverage as the particle is estimated to be lower than 80 nm.

The particles in Au_60 were found to be much smaller than what was planned, with a diameter of 36 nm $\pm$ 5 nm. This reduction in particle size reduced the surface coverage with 25 % and thus lowering the extinction maxima.

(A) Extinction spectra for Au_60.

(B) Absorption spectra for Au_60.
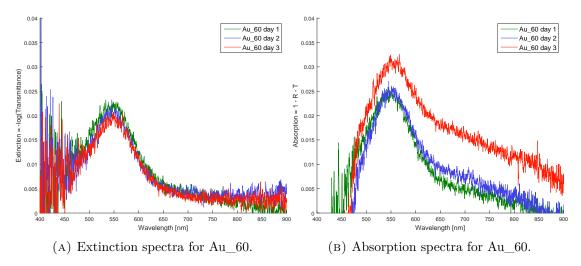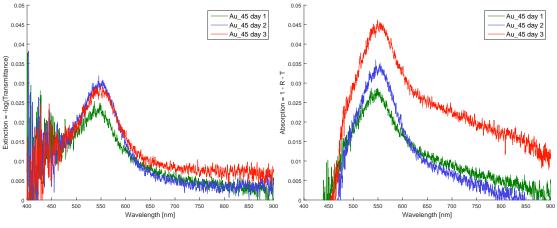
FIGURE 5.18: Measured extinction and absorption spectra for Au_60. The particles turned out to be around 30 nm instead of 60 nm. Drastically reducing the surface coverage and hence reducing the extinction/absorption.

Au_60 and Au_45 statistically are found to have similar particle size, with particles diameter 36 nm $\pm$ 5 nm and 34 nm $\pm$ 3 nm respectively. This is also confirmed in their similar extinction and absorption spectra, in both height (3.3 and 3.8 respectively) and peak position (562 nm $\pm$ 5 nm and 558 nm $\pm$ 2 nm respectively).

(A) Extinction spectra for Au_45.

(B) Absorption spectra for Au_45.

FIGURE 5.19: Measured extinction and absorption spectra for Au_45. Particles were found to be smaller than 45 nm, as a consequence the surface coverage was lowered from 7.07 % to 3.71 %. This leads to a low extinction/absorption spectra, but the distinct and quite narrow peak indicates a small size distribution.

In Figure 5.20 the extinction spectra for Al_200 is presented. In this spectrum, the peak is very broad, nearly covering the entire visible spectrum. This could be caused by a large variation of particle sizes within the array, causing it to become a mixed array instead of a single-sized particle array. However the particle size for the array was 192 nm $\pm$ 7 nm, the same standard deviation as for Au_200. This indicates that it is a property of aluminium to absorb over a wider band of wavelengths. The same broadened peaks can be seen for Al_150 and Al_120 supporting the proposed theory. Another possibility is that Al has a higher sensitivity to particle shape, and therefore a broader peak is experienced even with a standard deviation of 7 nm. Nonetheless, further research in the properties of aluminium nanoparticles are needed before a definite conclusion can be drawn.

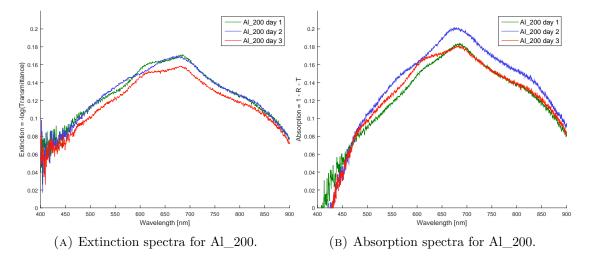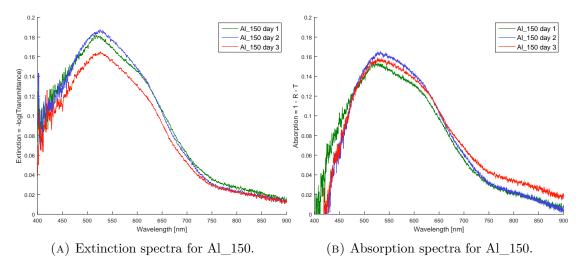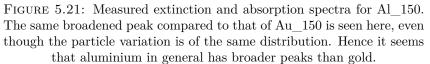(A) Extinction spectra for Al_200.

(B) Absorption spectra for Al_200.

FIGURE 5.20: Measured extinction and absorption spectra for Al_200. The spectrum for Al_200 is very broad, however particle size and shape distribution is small indicating that aluminium behaves differently compared to gold.

The maximum extinction value was found to be 17 %, which is 30 % lower than for Au_200, but there is only a 5 % difference in surface coverage between the two arrays. Thus it seems like gold in general is a more efficient absorber than aluminium.

Au_150 shown in Figure 5.21 continues the tendency of a broad peak for aluminium particles as seen for Al_200. When comparing it to the extinction spectra for Au_150 in Figure 5.14 it becomes especially clear that the peak is broadened. As already mentioned, the size distribution within the array is quite small and makes it difficult to pinpoint the reason behind the broad peak.

(A) Extinction spectra for Al_150.   (B) Absorption spectra for Al_150.

FIGURE 5.21: Measured extinction and absorption spectra for Al_150. The same broadened peak compared to that of Au_150 is seen here, even though the particle variation is of the same distribution. Hence it seems that aluminium in general has broader peaks than gold.

The difference in surface coverage between Al_150 and Au_150 is a 5 % increase. However the extinction maxima is at 29 % for Au_150 but only 17 % for Al_150. A similar decrease was seen when comparing Au_200 to Al_200, implying an advantage in using gold as the metal for solar absorbers.

The trend of broad aluminium peaks are continued in Figure 5.22 presenting the extinction and absorption spectra for Al_120. However, the peak is narrower than those for the Al_arrays of larger particle size. Al_120 cannot directly be compared to Au_120 as the gap between particle size and surface coverage is too large. However the general shapes of the peaks can be compared, as the standard deviation of the arrays are of the same order and it is seen that the peak is broader for Al_120 compared to that of Au_120.

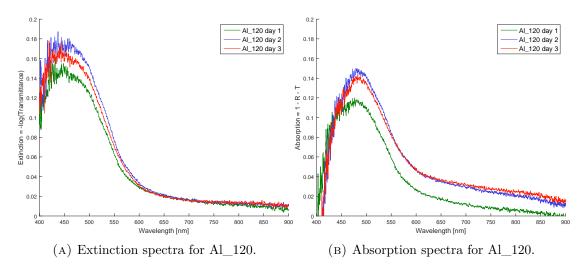(A) Extinction spectra for Al_120.

(B) Absorption spectra for Al_120.

FIGURE 5.22: Measured extinction and absorption spectra for Al_120.
The noise on the left of the extinction spectra is due to spectral rang of
the light source and spectrometer.

All of the aluminium arrays are blueshifted compared to their respective gold array, which is a known property of aluminium [37]. That is why making a solar absorber based on both gold and aluminium particles could cover the entire spectra. The experimental extinction spectra and peak positions along with the calculated surface coverage and extinction efficiencies for the single particle arrays are presented in Table 5.8. Due to the high discrepancy in peak height for the extinction spectra based on sub-optimum placement of the array in the integrated sphere, the highest peak values was chosen to represent the array, and the width of the plot line is defined as error bars

TABLE 5.8: Optical properties for the single particle arrays found
through SEM characterisation. The errors were found as standard de-
viations. Surface coverage and extinction efficiencies for Au_80 are not
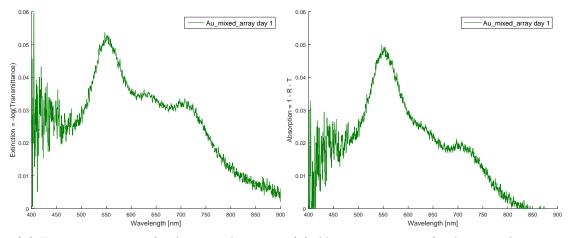calculates since measured interparticle distances were not obtained.

	Extinction [%]	SC [%]	Extinction Efficiency	Peak positions [nm]
Au_200	23.0 ± 0.2	8.2 ± 0.1	2.8 ± 0.1	815 ± 7
Au_150	29.0 ± 0.2	8.5 ± 0.2	3.4 ± 0.1	702 ± 2
Au_120	15.0 ± 0.2	4.5 ± 0.1	3.3 ± 0.1	615 ± 3
Au_100	20.0 ± 0.2	8.0 ± 0.3	2.5 ± 0.1	587 ± 1
Au_80	2.0 ± 0.5			550 ± 5
Au_60	2.0 ± 0.5	3.3 ± 0.2	0.6 ± 0.2	562 ± 5
Au_45	3.0 ± 0.5	3.8 ± 0.1	0.8 ± 0.1	558 ± 2
Al_200	17 ± 0.2	7.8 ± 0.1	2.18 ± 0.04	680 ± 5
Al_150	17 ± 0.2	8.1 ± 0.1	2.09 ± 0.04	557 ± 1
Al_120	18 ± 0.2	7.5 ± 0.1	2.41 ± 0.05	455 ± 4

The extinction peaks and their positions were found through data analyses of the collected spectra. The drastic drop in extinction from Au_100 to Au_80 and the smaller arrays are due to the corresponding drop in surface coverage, reducing the amount of matter to interact with incoming photons. Strangely enough the extinction efficiency is

also quite low for those arrays, the most plausible explanation for this is that the actual surface coverage was less than assumed, in other words, a too high surface coverage is used in the calculations of the extinction efficiencies. The adhesion of small nanoparticles will be less than for the bigger nanoparticles, indicating that a larger loss of particles could be experienced for the smaller particle arrays. Results from other groups like Langhammer et al. [41] argue that even the smaller particles should achieve a high extinction, these results are based on measurements on smaller arrays.

5.3.2 Analysis of Mixed Arrays

Figure 5.23 shows the extinction and absorption spectra for Au_mixed_array which contains the gold particles planned for the solar absorber. As the array only contains the gold particles intended for the solar absorber, the surface coverage is rather low. Therefore, the extinction maxima itself is not that interesting. Instead we look at the shape of the extinction/absorption peak. There is three clear peaks within the extinction spectra showcasing the effect of a multiple particle array, where the different particle sizes absorbs a broader range of wavelengths. Based on the extinction measurements for Au_60 and Au_80, the extinction peak around 550 nm is expected as a majority of the particles are in the range of 30 nm to 80 nm. The last peak at roughly 700 nm is due to the large particle with a diameter of 163 nm ± 10 nm. The peak is in agreement with the results for Au_150.
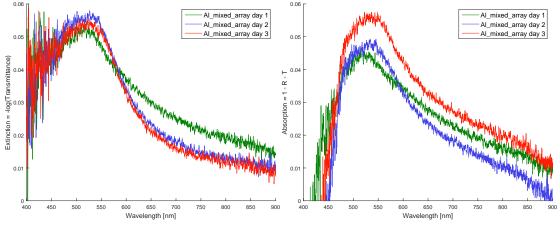

(A) Extinction spectra for Au_mixed_array.   (B) Absorption spectra for Au_mixed_array.

FIGURE 5.23: Measured extinction and absorption for Au_mixed_array. As expected low extinction values due to the low surface coverage. Several distinct peaks and very broad spectra showcasing the effect of varied particle sizes. Only one measurement was made on this sample as it was used as the basis for Au_Al_mixed_array sample to save time.

In the absorption spectra the middle peaks seems to flatten out a bit, this is probably due to an increase in scattering interactions in that region. The peak is also strongest in the area around 550 nm, hence the smaller particles seem to dominate the spectra. This is rather interesting as the combined surface coverage for the smaller particles is lower than that for the 160 nm particles. This implies that the combined extinction efficiency of the smaller particles is higher than that of the 163 nm ± 10 nm particles.

Figure 5.24 contains the spectra for the Al_mixed_array. As expected it is dominated by the two larger particles 133 nm ± 12 nm and 144 nm ± 11 nm. If compared
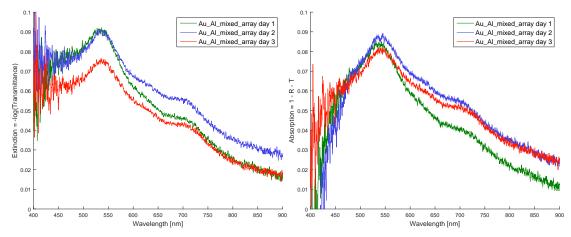
to the spectra of Al_150 in Figure 5.21 a similarity in shape is seen. However the maximum extinction is much lower due to the difference in surface coverage.

(A) Extinction spectra for Al_mixed_array   (B) Absorption spectra for Al_mixed_array

FIGURE 5.24: Measured extinction and absorption for Al_mixed_array.
Low surface coverage gives a low extinction. A broad peak indicating
that the particles chosen absorbs over a wide range of wavelengths

The broad peak compared to Al_120 and Al_150 indicates that all of the particles contribute to the extinction, although the larger ones dominates. Thus it is an optimizing problem regarding particle distribution to get the wanted peak shape. Interparticle distance and array structure also need to be optimized to achieve a higher surface coverage, and thus a higher extinction.

The measured extinction and absorption spectra for Au_Al_mixed_array are shown in Figure 5.25. This array was constructed through overlap and contains both gold and aluminium particles. SEM images could not be obtained for this array within the timeframe of this theis work due to instrument down-time. However, an improvement in extinction and absorption is seen when compared to Au_mixed_array and Al_mixed_array. In theory should the combined spectra from Au_mixed_array and Al_mixed_array result in the measured Au_Al_mixed_array. However a small deviation due to particle shifts and near-field coupling would be expected. Hence the peak in the range 525 nm - 575 nm is expected, as this is where both Au_mixed_array and Al_mixed_array had their peak maxima. The right side of the peak is similar to that of the Au_mixed_array peak, as this is where the gold particles are anticipated to absorb. The contribution from the aluminium particles are seen as the peak is broadened further to the left compared to that of Au_mixed_array.
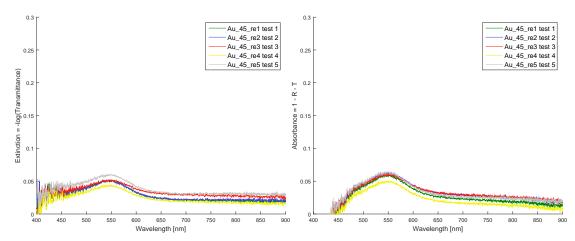
(A) Extinction spectra for Au_Al_mixed _ar-
ray.

(B) Absorption spectra for Au_Al_mixed _ar-
ray.

FIGURE 5.25: Measured extinction and absorption spectra for
Au_Al_mixed_array. The surface coverage is quite low for the individual
particles resulting in a low efficiency. The spectrum does show absorption
over the entire visible light spectrum as the goal was to achieve. Several
peaks are seen as well.

The result of the Au_Al_mixed_array shows a low achieved extinction due to the
low surface coverage in the array (less than 1% for each particle size). The broadened
peak is a indication of variation in particle size as expected, showing that it is possible to
use MNPs to absorb wavelengths over a broad spectrum. Although the achieved extinc-
tion is low the results showcase the potential of a solar absorber built on this technology.

As seen in the above extinction and absorption spectra there is a discrepancy between
the measurements made at different days. To investigate this further 5 additional mea-
surements were done for two samples, Au_200 and Au_45. The samples were taken
in and out of the sphere after every measurement to simulate the effect of doing it on
different days. In addition extra precaution were taken to ensure that the sample was
placed in the same spot everytime. The results are presented in Figure 5.26.

(A) Five different extinction spectra for Au_45. (B) Five different absorption spectra for Au_45.

(C) Five different extinction spectra for
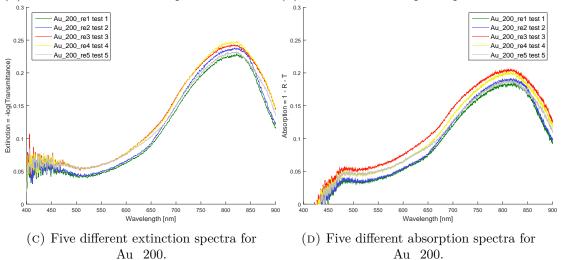Au_200.

(D) Five different absorption spectra for
Au_200.

FIGURE 5.26:   Reproducibility test for the integrated sphere setup.
Au_45 and Au_200 were tested 5 times in a row, the sample was taken
out of the spheres between each measurement. Effort was put into placing
the sample in the same spot everytime.

The overlap between the different spectra are not perfect, but it is a clear improvement compared to Figure 5.13a, 5.13b, 5.19a and 5.19b. Hence the variation in the measured spectra can be attributed to the positioning of the sample, where a small deviation in placement could influence the final spectra. The order in which the spectra are taken does not seem to be of any influence as it varies in Figure 5.26, which is the spectrum with the highest peak. An increase in the maximum extinction peak is also experienced for the Au_45 array, further proving the importance of sample placement in the integrating spheres.

As mentioned in Section 2.4 absorption is found through conservation of energy. To verify that our integrating sphere system does not lose more energy than expected, R + T + A were plotted in Figure 5.27.
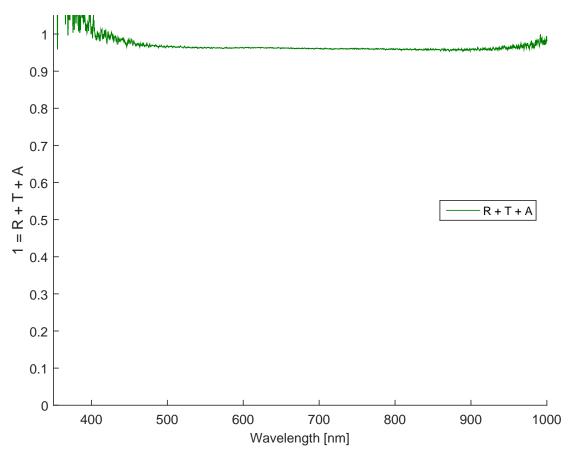
FIGURE 5.27: Energy conservation ensures that R + T + A = 1, however there is clearly a energy loss in the spheres. This is due to the imperfect reflection coating on the inside of the spheres and in general there is a energy loss through the sample ports of the spheres.

There seems to be a energy loss as our equation does not equal one. The imperfect reflective coating should be accounted for in the data processing. However, dust and other contamination could influence the final reflection. The main contributor is the light lost through the open ports (sample ports etc.) of the spheres and the fact that they are not coated in the reflective material. The loss from the sample ports is challenging to quantify as the spatial distribution of the scattered light is not known [41]. To minimize these losses the surface area of the sample ports should be as small as possible, less than 5 % of the total internal area of the spheres. The R, T and A values in Figure 5.27 are based on the Au_150 spectra, however similar graphs were plotted for the remaining arrays as well to make sure energy was conserved. These figures are not presented, as Figure 5.27 is representative for the others.

Another way to evaluate the MNP's optical properties are through the extinction efficiency. Using equation (2.44) we see that the extinction of the MNPs are proportional to the surface coverage and the extinction efficiency. The extinction efficiency is individual for each MNP and is given as the optical cross section divided on the geometrical cross section of the particle, as seen in Eq 2.44. In other words it says something about the size of the area in which the particles are expected to be optically active. It should be noted that the optical cross section is wavelength dependent, this is further discussed in Section 2.2.1. Simply said an extinction efficiency of 5 for a particle with diameter

100 nm would mean that absorption/scattering would occur within a circle with a diameter of 500 nm. Therefore, it is possible, in principle to achieve complete extinction with less than 100 % surface coverage. By extracting the extinction values from the obtained spectra the extinction efficiency of the individual particles could be calculated. These values contain information about which particles sizes would be the most efficient independent of surface coverage. In other words, which particles would take up less space in the array and still provide a high contribution to the extinction.

In Figure 5.28 extinction based on equation (2.44) is plotted as a function of surface coverage. The given extinction efficiency values are obtained through calculations based on the obtained spectra. The figure shows what surface coverage would be needed for each of the particles to achieve a given extinction.
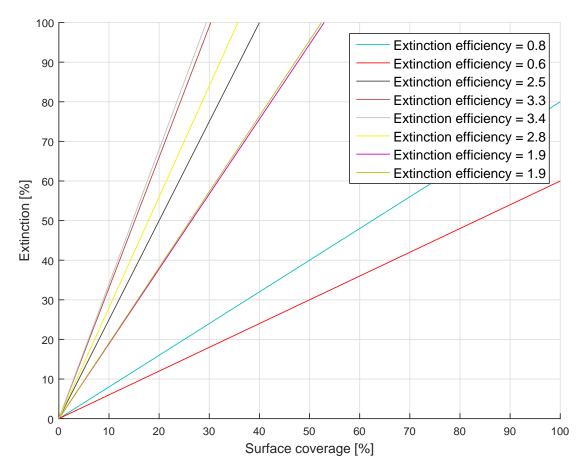

FIGURE 5.28: Extinction plotted against the surface coverage for the obtained extinction efficiencies.

With the current extinction efficiencies it is clear that the surface coverage has to increase if an improvement in extinction is to be expected. All of the arrays were made with three times the diameter as interparticle distance to avoid near-field coupling, if this limit could be pushed without compromising the LSPR a higher surface coverage could be achieved. Near-field coupling is a well known issue and deeply researched field, hence it is known that particles experiencing near-field coupling will have their resonance peak shifted. Thus by reducing the interparticle distance into the near-field coupling regime becomes an optimisation problem, where the advantage of increased surface coverage goes up against influence of near-field couplings.

A perfect solar absorber absorbs the entire visible light spectrum. Therefore particle composition is important as particle diameter affects the extinction. In Figure 5.29 and Figure 5.30 the extinction peak positions are plotted against particle diameter. In addition to the results from this thesis, results from other literature is also plotted. These results are taken from graphs in the corresponding articles. In the case of Greve et al. [30] the values were taken from tables. For the data collected from graphs the error bars was set to $\pm$ 30 nm. In their work Langhammer et al. [41] shown as blue diamonds, used nanoparticles with a height of 20 nm. Greve et al. [30] shown as yellow circles, used nanoparticles with a height of 25 nm, Temple et al. [37] shown as orange triangles, used nanoparticles with a height of 40 nm resulting in a blue shift of the peak position with regards to the positions obtained in this thesis [54]. Niklasson et al. [55] and Rechberger et al. [46] used 15 nm and 17 nm as nanoparticle height respectively, leading to a red shift compared to the 20 nm height is in this work [54].
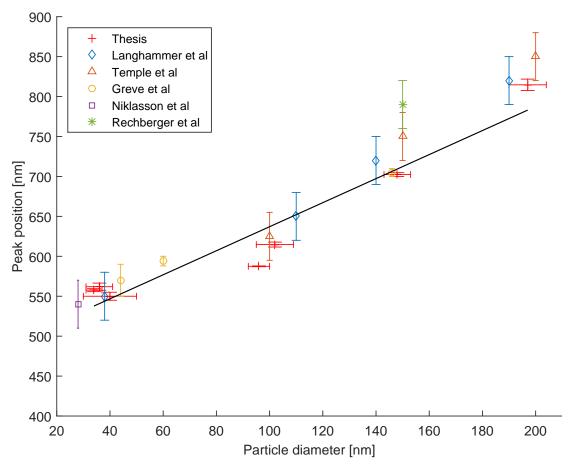

FIGURE 5.29: Peak position of the extinction spectra plotted against corresponding particle diameter for gold.
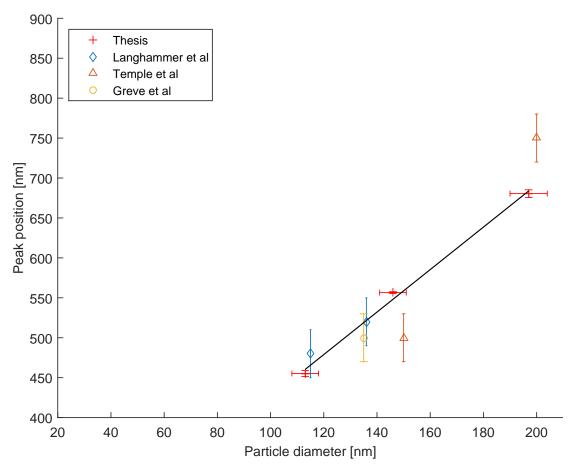
FIGURE 5.30: Peak position of the extinction spectra plotted against corresponding particle diameter for aluminium.

The results presented in Figure 5.29 and Figure 5.30 fit well with an overall trend and the expected shift of the LSPR with particle size is clear. The straight line in Figure 5.29 and Figure 5.30 is a linear fit of the data points found in this work. This is in agreement with Mie theory [33], which predicts a linear relationship between peak position and particle size [56].

As previously mentioned another important property of MNPs is their extinction efficiency, which says something about how efficient the MNPs will absorb/scatter the incoming radiation. The extinction efficiencies for the MNPs are plotted as a function of particle diameter in Figure 5.31. As seen in Figure 5.31 larger particles seems to have a higher extinction efficiency, though this number has to be taken with some reservation, since the low numbers for the smaller particles may be due to a wrongly estimated surface coverage. At any rate since the peak position is shifted for aluminium relative to gold, the best solar absorber would be made by mixing larger gold and aluminium particles.
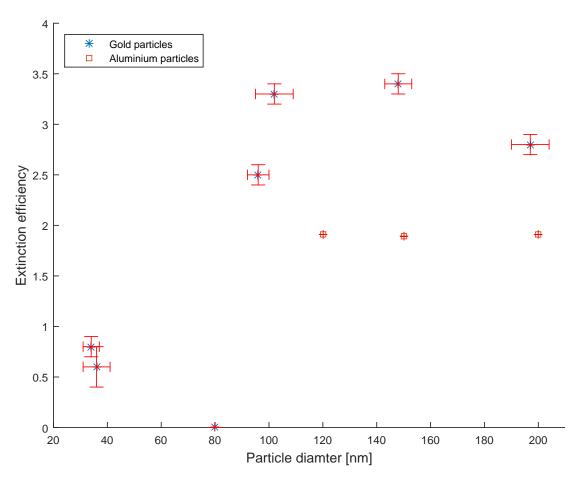
FIGURE 5.31: The measured extinction efficiencies plotted against the particle diameters for gold and aluminium. There are some doubts as to the validity of the numbers for the smallest nanoparticles as discussed in the main text.

Chapter 6

Conclusion and Future Work

The overall objective of this work was to determine the optimum arrangement of metal nanoparticles on a glass substrate for absorbing the largest part of the visible spectrum. In the work presented here metal nanoparticles of gold and aluminium were investigated. In addition, a fabrication method for arrays containing several metals and nanoparticles with varying diameter was to be established. Large single particle arrays and mixed arrays were produced by the means of EBL, and their optical properties were investigated by an integrating sphere setup. Structural characterisation based on SEM images showed that the largest particle arrays (D > 120 nm) were produced with the correct particle diameter and interparticle distance. However, the arrays containing smaller particles (D < 120 nm) were consistently produced with a diameter smaller than the design parameter. Further optimization of EBL writing parameters could reduce this discrepancy, but not remove it completely. Another issue that requires further attention is the tilt caused by what is believed to be the clips holding the sample in place on the sample holder. In addition to the thin substrates used. In order to produce large arrays with a narrow particle distribution, this effect must be minimised. This can either be done through further research into the tilt compensating tool within the e_Line software, or by introducing a more sturdy substrate which is not distorted by the mounting in the sample holder. Such a substrate was tried out in this work. However, the adhesion between the MNPs and the substrate was found to be poor and as a result none of the attempted 45 nm particles stayed on the surface after lift-off. Au_45 was made with the same EBL writing parameters on a regular substrate afterwards. This confirmed that the lack of particles was not related to a low exposure dose.

   The results from the optical analyses confirmed the high size dependency of the LSPR peak, which is also predicted by theory, and has been observed in work published by this and other groups. Our results can be used to fabricate an array consisting of particles with varying diameter which would absorb electromagnetic radiation over the whole spectrum. Furthermore, a high correlation between surface coverage and extinction maxima was seen. This demonstrates the importance of a high surface coverage when the aim is to achieve a considerable extinction. The mixed arrays produced in this work had a noticeable low surface coverage due to the minimum interparticle distance needed to avoid near-field coupling between the particles. This resulted in a low extinction peak. It can therefore be concluded that research should be directed towards the idea of utilising and controlling the near-field coupling with regards to the LSPR peak. Rechberger et al. [46] found that the near-field coupling would either redshift or blueshift the peak position depending on the polarisation of the incoming light. By investigating how the near-field coupling influences the LSPR peak position as a function of interparticle distance and particle diameter, it could in the future be possible to utilise near-field coupling as a LSPR peak adjustment tool. Another way to increase the surface coverage that should be pursued is to use a hexagonal structure instead of the simple cubic pattern, as the

hexagonal structure provides the closest packing of particles in 2D. Implementing varying particle diameters and interparticle distances could provide an issue, nonetheless an attempt should be made to implement it in a mixed array design. The two metals used in the fabrication of the MNP arrays exhibits similar trends in their LSPR properties, however two differences are clearly seen as described in Chapter 5. Firstly the aluminium peaks are clearly blueshifted relative to their gold counterparts, previously documented in the literature [37][41]. Secondly the aluminium peak is much broader than that of gold. Based on the optical results it could be concluded that Al_200 would be a suitable candidate for the solar absorber. The Al_200 array is a single particle array with 192 nm $\pm$ 7 nm aluminium particles. The extinction peak of this particular array is very broad, nearly covering the entire visible spectrum. However, a clear maximum is seen in Figure 5.20 and the extinction falls off further away from the peak position. Therefore, a mixed particle array with 200 nm aluminium particles together with smaller aluminium particles (60 nm - 150 nm) could absorb the entire visible spectra with high efficiency. Further research should be done towards the particle size sensitivity for aluminium particles. As the broad peak could also be explained by a high sensitivity towards size variations within the array.

Unfortunately a slight variation between measurements taken at different times with the integrating sphere setup was seen. This is attributed to the difficulties in placing the array in the same spot every time. This was especially difficult for the arrays with particles smaller than 100 nm as the arrays were hard to see on the substrate. A possible solution to this is to increase the size of the array, this would reduce the importance of perfect placement in the integrating spheres. However this would also increase the fabrication time for the arrays, which for some of the arrays would mean fabrication time off more than 24 hours. A more viable solution would be to improve the setup itself, perhaps by using a more focused light spot.

Based on the results obtained in this work it is clear that a solar absorber based on MNPs is viable and could be produced with the current available technology. Two things will be the main concern when finalizing the solar absorber design, surface coverage and LSPR peak position. It is clear that the surface coverage heavily influences the maximum extinction achieved and therefore a hexagonal structure is best suited as the foundation for the EBL pattern. The LSPR peak position will determine the absorption range of the solar absorber. Hence particles should be chosen in a way that the entire spectrum is absorbed. As seen for gold and aluminium it is clear that gold absorbs in the 500 nm - 800 nm range while aluminium absorbs in the 400 nm - 700 nm range. By utilising these two metals together it is possible to create an array based on MNPs with diameters above 100 nm which will absorb over the entire visible spectrum. This will avoiding the more complicated process of creating small nanoparticles. However the exact particle distribution requires further optimisation before a "perfect" solar absorber can be produced.

A process for creating arrays consisting of both gold and aluminium particles were developed. However SEM images of the Au_Al_mixed_array could not be obtained due to downtime in the UiB nanostructures laboratory. Therefore, the procedure was only tested on 500 µm $\times$ 500 µm arrays. The results were promising and the procedure should be optimised further through a complete understanding of the e_Line software's 3-point alignment tool.

Bibliography

[1]   Unfccc. "Draft decision - / CP . 15". In: *Conf. Parties to Clim. Chang. Conv.* (2009): pp. 1–5.

[2]   T. F. Stocker et al. "IPCC, 2013: Summary for Policymakers." In: *Clim. Chang. 2013 Phys. Sci. Basis. Contrib. Work. Gr. I to Fifth Assess. Rep. Intergov. Panel Clim. Chang.* (2013).

[3]   United Nations. "Adoption of the Paris Agreement". In: *Conf. Parties its twenty-first Sess.* 21932 (December) (2015): p. 32.

[4]   "BP Statistical Review of World Energy 2014". In: ().

[5]   R. Schmalensee et al. "The Future of Solar Energy". In: *MIT Energy Initiat. "Future of"* ().

[6]   V. Fthenakis. "Sustainability of photovoltaics: The case for thin-film solar cells". In: *Renew. Sustain. Energy Rev.* 13 (9) (2009): pp. 2746–2750.

[7]   M. A. Green. "Photovoltaic principles". In: *Phys. E Low-Dimensional Syst. Nanostructures*, 14 (1-2) (2002): pp. 11–17.

[8]   T. M. Razykov et al. "Solar photovoltaic electricity: Current status and future prospects". In: *Sol. Energy*, 85 (8) (2011): pp. 1580–1608.

[9]   P. Hofmann. *Solid-state physics.* Wiley-VCH Verlag GmbH & Co, 2008.

[10] C. Kittel. *Introduction to Solid State Physics.* 8th. John Wiley & Sons, 2005, p. 680. ISBN: 0471111813.

[11] W. Shockley and H. J. Queisser. "Detailed Balance Limit of Efficiency of p-n Junction Solar Cells". In: *J. Appl. Phys.* 32 (3) (1961): p. 510.

[12] D. A. Kleinman. "Considerations on the solar cell". In: (1960): pp. 85–115.

[13] D. M. Chapin, C. S. Fuller, and G. L. Pearson. "A new silicon p-n junction photocell for converting solar radiation into electrical power". In: *J. Appl. Phys.* 25 (5) (1954): pp. 676–677.

[14] M. A. Green. "Third generation photovoltaics: Solar cells for 2020 and beyond". In: *Phys. E Low-Dimensional Syst. Nanostructures*, 14 (1-2) (2002): pp. 65–70.

[15] M. A. Green and S. Pillai. "Harnessing plasmonics for solar cells". In: *Nat. Photonics*, 6 (3) (2012): pp. 130–132.

[16] M. Mazzer et al. "Progress in quantum well solar cells". In: *Thin Solid Films*, 511-512 (2006): pp. 76–83.

[17] L. El Chaar, L. A. Lamont, and N. El Zein. "Review of photovoltaic technologies". In: *Renew. Sustain. Energy Rev.* 15 (5) (2011): pp. 2165–2175.

[18] N. M. Gabor et al. "Extremely Efficient Multiple Electron-Hole Pair Generation in Carbon Nanotube Photodiodes". In: *Science*, 325 (5946) (2009): pp. 1367–1371.

[19] T. K. Manna and S. M. Mahajan. "Nanotechnology in the development of photovoltaic cells". In: *2007 Int. Conf. Clean Electr. Power, ICCEP '07* (2007): pp. 379–386.

[20] A. Luque and A. Martí. "Increasing the Efficiency of Ideal Solar Cells by Photon Induced Transitions at Intermediate Levels". In: *Phys. Rev. Lett.* 78 (26) (1997): pp. 5014–5017.

[21] R. Ehrlich. *Renewable Energy.* CRC Press, 2013.

[22] J. B. Chou et al. "Enabling ideal selective solar absorption with 2D metallic dielectric photonic crystals". In: *Adv. Mater.* 26 (47) (2014): pp. 8041–8045.

[23] Youngsuk Nam et al. "Solar thermophotovoltaic energy conversion systems with two-dimensional tantalum photonic crystal absorbers and emitters". In: *Sol. Energy Mater. Sol. Cells*, 122 (2014): pp. 287–296.

[24] A. Lenert et al. "A nanophotonic solar thermophotovoltaic device". In: *Nat. Nanotechnol.* 9 (2) (2014): pp. 126–130.

[25] S. A. Maier. *Plasmonics: Fundamentals and Applications.* Boston, MA: Springer US, 2007, p. 223. ISBN: 978-0-387-33150-8. arXiv: *0405528* [cond-mat].

[26] H. A. Atwater and A. Polman. "Plasmonics for improved photovoltaic devices." In: *Nat. Mater.* 9 (3) (2010): pp. 205–213.

[27] N. Liu et al. "Infrared perfect absorber and its application as plasmonic sensor". In: *Nano Lett.* 10 (7) (2010): pp. 2342–2348.

[28] K. Aydin et al. "Broadband polarization-independent resonant light absorption using ultrathin plasmonic super absorbers". In: *Nat. Commun.* 2 (2011): p. 517.

[29] Ranveig Flatabø. "Optical Properties of Metal Nanoparticle Arrays created using Electron Beam Lithography for Solar Cell Applications". In: (June) (2014).

[30] M.M. Greve, T. O. Håvardstun, and B. Holst. "Measuring the localized surface plasmon resonance effect on large arrays (5 mm x 5 mm) of gold and aluminium nanoparticles on borosilicate glass substrates, fabricated by electron beam lithography". In: *J. Vac. Sci. Technol. B*, 31 (6) (2013).

[31] I. Freestone et al. "The Lycurgus Cup - A Roman nanotechnology". In: *Gold Bull.* 40 (4) (2007): pp. 270–277.

[32] M. Garnett. "Colours in Metal Glasses and in Metallic Films". In: *Philos. Trans. R. Soc. London*, 203 (1904): pp. 385–420.

[33] G. Mie. "Contributions to the optics of turbid media, particularly of colloidal metal solutions". In: *Ann. Phys.* 25 (3) (1908): pp. 377–445.

[34] D. Pines. "Collective energy losses in solids". In: *Rev. Mod. Phys.* 28 (3) (1956): pp. 184–198.

[35] R. H. Ritchie. "Plasma Losses by Fast Electrons in Thin Films". In: *Phys. Rev.* 106 (5) (1957): pp. 874–881.

[36] U. Kreibig and P. Zacharias. "Surface Plasma Resonances in Small Spherical Silver and Gold Particles". In: *Z. Phys.* 143 (231) (1970): pp. 128–143.

[37] T. L. Temple and D. M. Bagnall. "Optical properties of gold and aluminium nanoparticles for silicon solar cell applications". In: *J. Appl. Phys.* 109 (8) (2011).

[38] T. O. Håvardstun. "Optical Properties of Metal Nanoparticle Arrays created using Electron Beam Lithography". In: (June) (2013).

[39] D. J. Griffiths. *Introduction to Electrodynamics.* Pearson Education Limited, 2014, pp. 1–604.

[40] E. Hutter and J. H. Fendler. "Exploitation of localized surface plasmon resonance". In: *Adv. Mater. (Weinheim, Ger.* 16 (19) (2004): pp. 1685–1706.

[41] C. Langhammer, B. Kasemo, and I. Zorić. "Absorption and scattering of light by Pt, Pd, Ag, and Au nanodisks: Absolute cross sections and branching ratios". In: *J. Chem. Phys.* 126 (19) (2007).

[42] E. Hecht. *Optics.* Fourth. Pearson Education, 2002.

[43] C. F. Bohren and D. R. Huffmann. *Absorption and Scattering of Light by Small Particles.* New York: Wiley, 1983.

[44] D. Sarkar and A. Haldar. *Physical and Chemical Methods in Soil Analysis.* New Age International Pvt Ltd Publishers, 2010. ISBN: 8122427257.

[45] W. Gotschy et al. "Thin films by regular patterns of metal nanoparticles: tailoring the optical properties by nanodesign". In: *Appl. Phys. B Lasers Opt.* 63 (4) (1996): pp. 381–384.

[46] W. Rechberger et al. "Optical properties of two interacting gold nanoparticles". In: *Opt. Commun.* 220 (1-3) (2003): pp. 137–141.

[47] M. A. Yurkin and A. G. Hoekstra. "The discrete dipole approximation: An overview and recent developments". In: *J. Quant. Spectrosc. Radiat. Transf.* 106 (1-3) (2007): pp. 558–589. arXiv: *0704.0038*.

[48] R. Lazzari and I. Simonsen. "GRANFILM: A software for calculating thin-layer dielectric properties and Fresnel coefficients". In: *Thin Solid Films*, 419 (1-2) (2002): pp. 124–136.

[49] M. M. Greve. "Nanostructures for the manipulation of electromagnetic waves". In: (September) (2013): pp. 17–28.

[50] M. A. Mohammad et al. "Nanofabrication". In: (2012).

[51] J. Z. Zhang. *Optical Properties and Spectroscopy of Nanomaterials.* World Scientific Publishing Co. Pte. Ltd., 2009, p. 383. ISBN: 9789812836663.

[52] P. K. Jain et al. "Calculated absorption and scattering properties of gold nanoparticles of different size, shape, and composition: applications in biological imaging and biomedicine." In: *J. Phys. Chem. B*, 110 (14) (2006): pp. 7238–48.

[53] K. L. Kelly et al. "The Optical Properties of Metal Nanoparticles: The Influence of Size, Shape, and Dielectric Environment". In: (2002): pp. 7178–7186.

[54] U. Guler and R. Turan. "Effect of particle properties and light polarization on the plasmonic resonances in metallic nanoparticles." In: *Opt. Express*, 18 (16) (2010): pp. 17322–17338.

[55] G. A. Niklasson and H. G. Craighead. "Optical response and fabrication of regular arrays of ultrasmall gold particles". In: *Thin Solid Films*, 125 (1985): pp. 165–170.

[56] S. Link and M. A. El-Sayed. "Spectral Properties and Relaxation Dynamics of Surface Plasmon Electronic Oscillations in". In: *J. Phys. Chem. B*, 103 (1) (1999): pp. 8410–8426.